Journal of Molecular Structure 991 (2011) 108–126

Contents lists available at ScienceDirect

Journal of Molecular Structure

journal homepage: www.elsevier.com/locate/molstruc

Palladium(II) and platinum(II) complexes containing benzimidazole ligands: Molecular structures, vibrational frequencies and cytotoxicity

Nour T. Abdel Ghani *, Ahmed M. Mansour

Chemistry Department, Faculty of Science, Cairo University, Gamaa Street, Giza 12613, Egypt

ARTICLE INFO

Article history:
Received 3 November 2010
Received in revised form 12 January 2011
Accepted 7 February 2011
Available online 12 February 2011

Keywords:
Benzimidazole
Antitumor
NBO
Palladium complexes

ABSTRACT

(1H-benzimidazol-2-ylmethyl)-(4-methoxyl-phenyl)-amine (L^1), (1H-benzimidazol-2-ylmethyl)-(4-methyl-phenyl)-amine (L^2) and their Pd(II) and Pt(II) complexes have been synthesized as potential anticancer compounds and their structures were elucidated using a variety of physico-chemical techniques. Theoretical calculations invoking geometry optimization, vibrational assignments, ^{1}H NMR, charge distribution and molecular orbital description HOMO and LUMO were done using density functional theory. Natural bond orbital analysis (NBO) method was performed to provide details about the type of hybridization and the nature of bonding in the studied complexes. Strong coordination bonds (LP(1)N11 → σ*(M—Cl22)) and (LP(1)N21 → σ*(M—Cl23)) (M = Pd or Pt) result from donation of electron density from a lone pair orbital on the nitrogen atoms to the acceptor metal molecular orbitals. The experimental results and the calculated molecular parameters revealed square-planar geometries around the metallic centre through the pyridine-type nitrogen of the benzimidazole ring and secondary amino group and two chlorine atoms. The activation thermodynamic parameters were calculated using non-isothermal methods. The synthesized ligands, in comparison to their metal complexes were screened for their antibacterial activity. In addition, the studied complexes showed activity against three cell lines of different origin, *breast cancer* (MCF-7), *Colon Carcinoma* (HCT) and *human heptacellular carcinoma* (Hep-G2) comparable to cis-platin.

1. Introduction

Despite the widespread use of cis-diaminedichloroplatinum(II) (cis-platin) as an anticancer drug there is still scope for improvement, with respect to reduced toxicity [1], increased clinical effectiveness, broader spectrum of action, elimination of side effects (e.g., nausea, hearing loss, vomiting, etc.), increased solubility, and the ability to use them in combination with other drugs. The generation of new platinum complexes for this application was based on an early structure–activity relationship, which stated that potentially active complexes should be neutral and contain two inert amine ligands (with at least one N—H bond) in the *cis* orientation and two semilabile leaving groups [2] (one of the reasons for choosing the ligands under study). The NH group is responsible for important hydrogen-bond donor properties, either in the approach of the biological target or the final structure. Recently, interest was directed toward the developing cis-platin analogs which have heterocyclic amine ligands coordinated to the cyctotoxic platinum(II) moiety. Several platinum complexes with N-heterocyclic ligands such as imidazole, thiazole, benzimidazole, benzothiazole, and benzoxazole were reported [3]. The benzimidazole scaffold is a useful structural motif for displaying chemical functionality in biologically active molecules. Some of its derivatives have potent biological activities as antitumor [4], anti-HIV [5], anti-Parkinson [6], and antimicrobial [7] agents. At the same time, because of the coordination chemistry of azoles acting as ligands in transition metal compounds, the chelating ligands incorporating benzimidazole groups have been extensively studied in the context of modeling biological systems in recent years [8]. Our aim was to take into account all the previously mentioned properties of anticancer drugs and synthesize new platinum(II) and palladium(II) complexes of the benzimidazole ligands ($L^{1,2}$) (Fig. 1) that could be proved to be potent antitumor agents through characterization and elucidation of their structures using spectroscopic, thermal and conductance measurements. *Density functional theory* (DFT) calculations were done in order to correlate between the theoretical and experimental results.

2. Experimental

2.1. Synthesis of ligands ($L^{1,2}$) and their complexes

All chemicals used in the preparation and investigation of the present study were of reagent grade (Sigma, Merk). The precursor compound 2-chloromethylbenzimidazole was prepared and

* Corresponding author. Fax: +20 2 35728843.
E-mail address: noureta2002@yahoo.com (N.T. Abdel Ghani).

0022-2860/$ - see front matter © 2011 Elsevier B.V. All rights reserved.
doi:10.1016/j.molstruc.2011.02.014

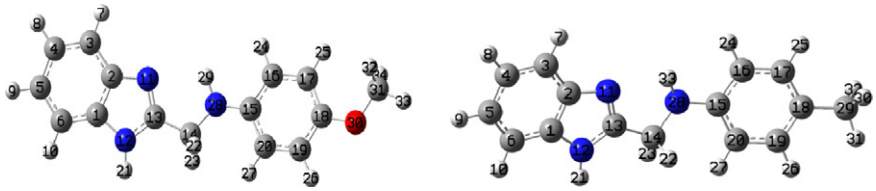

(L^1) (L^2)

Fig. 1. The optimized structures of the benzimidazoles L^1 and L^2.

recrystallized according to the previously reported methods [9]. The ligands $L^{1,2}$ were prepared by condensation of equimolar quantities of 2-chloromethylbenzimidazole with 4-methoxylaniline (L^1) and 4-methylaniline (L^2). The reaction mixture was refluxed in ethanol in presence of small amount of sodium iodide for about 18–24 h. At the end of the reaction period, the mixture was neutralized and the solid was separated by dilution with de-ionized water, and recrystallized from xylene and ethanol, respectively.

One millimole K_2PdCl_4 was prepared by dissolving 0.177 g of $PdCl_2$ in 0.149 g/50 mL aqueous KCl solution. The solid metal complexes of the benzimidazole compounds ($L^{1,2}$) with Pd(II), and Pt(II) metal ions were prepared by adding a hot ethanolic solution (60 °C) of the ligand (1 mmol) to a hot aqueous solution (60 °C) of the metal ions (1 mmol; K_2PdCl_4, or K_2PtCl_4). The resulting mixtures were stirred under reflux for about 1–2 h, whereupon the complexes, Pd–L^1 (**1**), Pt–L^1 (**2**), Pd–L^2 (**3**), and Pt–L^2 (**4**) were precipitated.

2.2. Instruments

Infrared spectra of the ligands and their complexes were recorded as potassium bromide disc using *FTIR-460 plus, JASCO, Japan*, in 4000–200 cm^{-1} region. The ^1H NMR spectra were run at 300 MHz using deuterated dimethylsulphoxide (DMSO-d_6) as a solvent and tetramethylsilane (TMS) as a reference using *Varian-Oxford Mercury VX-300 NMR*. Deuterium oxide (D_2O) was used to confirm the presence of ionizable protons. The mass spectra measurements were recorded with the aid of *SHIMADZU QP-2010 plus* mass spectrometer at 70 eV. The thermogravimetric analysis (TGA) and differential thermal analysis (DTA) were carried out by *DTG-60H SIMULTANEOUS DTA-TG APPARATUS-SHIMADZU* instrument in a dynamic nitrogen atmosphere (20 mL min^{-1}), with a heating rate of 10 °C min^{-1} using platinum crucible. Digital *Jenway 4330* Conductivity-pH meter with (1.02) cell constant was used for pH and molar conductance measurements. Spectrophotometric measurements were carried out using automated spectrophotometer UV/vis. *SHIMADZU Lambda 4B* using 1 cm matched quartz cells. The X-ray powder diffraction patterns of the benzimidazole L^2 and its Pd(II) and Pt(II) complexes were recorded over 2θ = 5–60° range using Philips X-ray diffractometer model PW 1840. Radiation was provided by copper anode (Kα, λ = 1.54056 Å) operated at 40 kV and 25 MA. Divergence slit and the receiving slit were 1 and 0.05, respectively.

2.3. Theoretical calculations

The molecular structures of the benzimidazoles ($L^{1,2}$) in the ground state were optimized by a DFT method using B3LYP functional [10,11] combined with 6-31G(d) and LANL2DZ basis sets. Calculations were carried out by GAUSSIAN 03 [12] suite of programs run on a PC workstation equipped with Pentium IV 3 GHz processor and 1 GB RAM memory. The vibrational frequencies of the benzimidazoles and the corresponding normal modes were evaluated at the optimized geometry [13] using the same basis sets. Vibrational modes were analyzed using GAUSSVIEW software [14]. The main reason in choosing the LANL2DZ basis set is its inclusion of relativistic effect that is essential for heavy elements e.g. Pd(II) and Pt(II), in order to compare between the optimized structures of the ligands and their complexes. The ^1H NMR chemical shifts of the benzimidazoles ($L^{1,2}$) were computed at the B3LYP/6-311 + G(2d,p) and B3LYP/LANL2DZ levels of theory in the gaseous state by applying the (GIAO) approach [15] and the values for the ^1H-isotropic were referenced to TMS, which was calculated at the same level of theory. The optimized structures, vibrational frequencies, ^1H-chemical shifts, and the natural bond (NBO) analysis of the metal complexes were obtained at B3LYP/LANL2DZ level of theory.

2.4. Biological activity

2.4.1. Antimicrobial activity

The antimicrobial activities of the test samples were determined using a modified Kirby-Bauer disc diffusion method [16] under standard conditions using *Mueller–Hinton* agar medium, as described by NCCLS [17]. The antimicrobial activities were carried out using culture of *Bacillus subtilis*, *Staphylococcus aureus, Streptococcus faecalis* as Gram-positive bacteria and *Escherichia coil*, *Pseudomonas aeruginosa*, *Neisseria gonorrhea* as Gram-negative bacteria. Briefly, 100 μL of the test bacteria were grown in 10 mL of fresh media until they reached a count of approximately 108 cells/mL. A 100 μL of microbial suspension was spread onto agar plates corresponding to the broth in which they were maintained. DMSO (0.1 mL) alone was used as control under the same conditions for each microorganism, subtracting the diameter of inhibition zone resulting with DMSO, from that obtained in each case. The results were compared with a similar run of *Tetracycline* as an antibacterial. The antimicrobial activities could be calculated as a mean of three replicates.

2.4.2. Cell culture and cytotoxicity determination

Three human cancer cell lines were used for *in vitro* screening experiments; *breast cancer* (MCF7),*Colon Carcinoma* (HCT) and *human heptacellular carcinoma* (Hep-G2). They were obtained frozen in liquid nitrogen (−180 °C) from the American Type Culture Collection. The tumor cell lines were maintained in the National Cancer Institute, Cairo, Egypt, by serial sub-culturing. Cell culture cytotoxicity assays were carried out as described previously [18]. RPMI-1640 medium was used for culturing and maintenance of the human tumor cell lines [18]. Cells were seeded in 96-well plates at a concentration of 5×10^4–10^5 cell/well in a fresh medium and left to attach to the plates for 24 h. Growth inhibition of cells was calculated spectrophotometrically using a standard method with the protein-binding dye sulforhodamine B (SRB) [19]. The results were compared with a similar run of *cis-platin* as an antitumor compound.

Table 1
Band assignment of experimental and theoretical FT-IR spectra of benzimidazole L[1].

No	Exp. freq	Calculated un-scaled frequency (B3LYP)		Scaled frequency uniform scaling		Scaled frequency linear regression scaling		Vibrational assignments
		6-31G(d)	LANL2DZ	6-31G(d)	LANL2DZ	6-31G(d)	LANL2DZ	
1		3649	3681	3514	3570	3538	3504	ν NH^{ss}/Bz
2	3428	3554	3616	3423	3507	3446	3442	ν NH^{ss}/An
3		3222	3231	3103	3134	3124	3075	ν CH^{ss}/An
4		3218	3238	3099	3140	3120	3082	ν CH^{ss}/Bz
5		3213	3226	3095	3129	3115	3071	ν CH^{ss}/An
6		3208	3224	3089	3127	3111	3069	ν CH^{ass}/Bz
7		3197	3206	3079	3109	3100	3052	ν CH^{ass}/An
8		3196	3209	3078	3112	3099	3054	ν CH^{ass}/Bz
9		3187	3196	3069	3100	3090	3042	ν CH^{ass}/Bz
10	3048	3178	3188	3060	3092	3081	3034	ν CH^{ass}/An
11	2999	3150	3177	3033	3081	3054	3024	ν CH_3^{ass}
12	2937	3069	3098	2956	3005	2976	2949	ν CH_3^{ass}
13		3015	3018	2903	2927	2923	2873	ν CH_3^{ss}
14		3001	2975	2890	2885	2910	2832	CH_2^{ass}
15	2832	2934	2957	2826	2868	2845	2814	CH_2^{ss}
16	1680	1687	1682	1625	1631	1635	1600	ν CC/An
17	1617	1683	1675	1621	1624	1631	1594	ν CC/Bz + ν C=N/Bz
19	1592	1643	1635	1582	1585	1593	1556	ν CC/Bz
20		1638	1626	1577	1577	1588	1547	ν CC/An + β NH^{sc}/An
21		1594	1581	1535	1533	1545	1504	ν C=N/Bz + β NH^{sc}/An + β NH^{sc}/Bz + $\delta_s CH_2$
22	1518	1573	1561	1515	1514	1525	1485	ν CC/An + CH_3^{opb} + $\delta_s CH_2$
23		1548	1530	1491	1484	1500	1456	β NH^{sc}/An + $\delta_s CH_2$
24		1544	1538	1487	1491	1497	1463	$\delta_s CH_2$
27		1537	1521	1480	1475	1490	1447	CH_3^{opb}
28		1535	1513	1478	1467	1488	1439	CH_3^{opb} + $\delta_s CH_2$ + ν CC/Bz
29	1456	1520	1512	1464	1466	1473	1438	CH_3^{ipb}
30		1501	1485	1446	1440	1455	1413	CH_3^{sb}
31		1497	1480	1442	1435	1451	1408	ν CC/Bz (boat shape)
		1046				1014		
32	1418	1474	1437	1419	1393	1429	1367	β CC/Bz + β CC/An + ω CH_2
36		1456	1431	1402	1388	1411	1361	ν CC/Bz + ω CH_2 + β NH^{sc}/An + β NH^{sc}/Bz + β CH/Bz + β CH/An
		1426		1373		1382		
37	1308	1352	1375	1303	1333	1310	1308	ν CC/An + β CH/Bz
40	1340	1349	1352	1299	1311	1307	1286	β CH/An
41		1334	1329	1285	1289	1293	1264	β CH/Bz + β CH/An + β NH^{sc}/An
42	1268	1317	1257	1268	1219	1276	1196	ν C—O/An + β CH/An + ω CH_2 + β CH/Bz + β NH^{sc}/An
44		1301		1253		1261		β CH/Bz + τCH_2 + β NH^{sc}/An
45	1232	1281		1234		1242		ν C—O/An + βCH/An + β NH^{sc}/An
46		1259	1226	1213	1189	1220	1166	τCH_2 + β NH/Bz + β CH/Bz
47		1247	1248	1201	1210	1209	1155	τCH_2
48	1179	1218	1193	1173	1157	1180	1135	CH_3^{opr} + βCH/Bz
49		1207		1162		1170		β NH/Bz + β CH/Bz + β CH/An
50		1212		1167		1175		β CH^{ss}/An
51		1187	1150	1143	1115	1150	1094	CH_3^{ipr}
52		1183		1139		1146		β CH/Bz
53	1124	1162	1167	1120	1131	1126	1110	ν CH_2—NH/An + β CH/An
	1096	1137		1095		1102		
54	1031	1086		1046		1052		ν C—O—CH_3
55		1038	1053	1000	1021	1006	1001	ρCH_2
		675				653		
		318	676		655	307	642	
56		1025	1017	987	986	993	967	Rtorsion/An
			657					
57		1023	1035	985	1004	991	984	Rtorsion/Bz
			1009		978		959	
58		912	908	877	880	883	863	Rtrigd/Bz
59	938	1143	982	1101	952	1108	934	γ CH/Bz
	820	973	896	937	869	942	852	
	749	930	799	896	775	901	760	
		861	786	830	762	834	747	
		776		748		752		
		757		729		733		
	716	589		567		570		
60	900	929	980	896	950	900	932	γ CH/An
		917	960	883	931	888	913	
		828	849	798	823	802	807	
		807	832	777	807	782	791	
			739		716		702	
61		787	761	758	738	762	723	Para deformation of aniline ring
62		658	871	634	844	637	828	Rtrigd/An

Table 1 (*continued*)

No	Exp. freq	Calculated un-scaled frequency (B3LYP)		Scaled frequency uniform scaling		Scaled frequency linear regression scaling		Vibrational assignments
		6-31G(d)	LANL2DZ	6-31G(d)	LANL2DZ	6-31G(d)	LANL2DZ	
63	617	632	634	608	614	612	602	Rtorsion/Bz
64		615	514	593	498	595	488	γ $NH_{anilino}$
65	432	437	592	421	574	422	562	γ NH_{Bz}
66		258	243	249	235	249	230	τCH_3

For 6-31G(d) basis set, the slope is equal 1.0310 and the linear coefficient is 0.9982.
For LANL2DZ basis set, the slope is equal 1.0500 and the linear coefficient is 0.9990.
R: ring; ss: symmetric stretching; ass: asymmetric stretching; ν, stretching; β, in-plane bending; γ, out-of-plane bending; ρ, rocking; ω, wagging; τ, torsion; trig: trigonal; trigd: trigonal deformation. ops: out-of-plane stretching; sb: symmetric bending; ipb: in-plane-bending; opb: out-of-plane bending; ipr: in-plane-rocking; opr: out-of-plane rocking.

3. Results and discussion

3.1. IR spectral studies

The theoretical IR spectra of the benzimidazole derivatives under study ($L^{1,2}$) were obtained at DFT/B3LYP level of theory using the 6-31G(d) and LANL2DZ basis sets. All the band assignments are presented in Tables 1 and 2. At this level, the calculated harmonic force constants and frequencies are higher than the corresponding experimental values, due to basis set truncation and neglecting of electron correlation and mechanical anharmonicity [20]. To compensate these shortcomings, scale factors were introduced and an explanation of this approach was discussed [21]. Two different methods were applied: (i) *uniform* scaling [21], the scaling factors are 0.963 for B3LYP/6-31G(d) and 0.970 for B3LYP/LANL2DZ methods (ii) *linear regression method* [22], in this method, the plot of the calculated frequencies versus their experimental values resulted in a straight line, whose equation was used to correct the calculated frequencies (ν_{calc}).

Benzimidazole derivatives ($L^{1,2}$) have a strong intermolecular hydrogen bond [3]; between the pyridine-type nitrogen, (N_3) and the benzimidazolic NH group; in the solid state, which makes the IR spectra show strong and broad absorption band in the region 3500–2200 cm^{-1}. It is not surprising to find this effect since benzimidazole and imidazole derivatives, possessing free imino hydrogen, are known to be capable of associating through hydrogen bond formation [23]. By using B3LYP/6-31G(d) method, the scaled calculated value at 3514 cm^{-1} is assigned to the benzimidazolic NH (NH_{Bz}) stretching vibration in the benzimidazoles ($L^{1,2}$). For Pt–L^1, Pd–L^2 and Pt–L^2 complexes (**2–4**), the $\upsilon(NH)_{Bz}$ bands are observed at 3225, 3227 and 3243 cm^{-1}, respectively, and are sharper than found in the uncoordinated ligand [3,24] due to the breaking of the intermolecular hydrogen bond. In Pd–L^1 complex (**1**), the $\upsilon(NH)_{Bz}$ vibration mode is embedded by the hydrogen bond effect generated by water of hydration. The theoretically scaled stretching mode of NH_{Bz} group in the benzimidazoles ($L^{1,2}$) and their complexes is found in the same position near 3570 cm^{-1} (Table 3). This reveals that the NH_{Bz} group remains intact in the complexes as found experimentally.

On the other hand, the presence of sharp bands at 3428 and 3434 cm^{-1}, respectively, in the spectra of the free ligands ($L^{1,2}$) indicated the existence of free secondary amino group (NH_{sec}) and these values coincide with the theoretically scaled modes, 3423 and 3428 cm^{-1}, respectively. These bands are still observed in the metal complexes, but they become broad and/or slightly shifted to lower frequency as shown in Table 3. This offers a proof that the NH_{sec} proton is not deprotonated [25] in the complex formation, whereas such shift and broadness reflect its involvement in coordination to the metal ions. This is confirmed theoretically by observing the computed stretching mode for the NH_{sec} group at lower wavenumbers than that of the free ligand.

The stretching vibrational mode of C=N bond in benzimidazole L^1 is in agreement with those of Mohan and Sundaraganesan [26] and Sundaraganesan et al. [27]. The band at 1680 cm^{-1} is assigned to υ(C=N) and is in a good agreement with the un-scaled calculated mode, 1687 cm^{-1}. It is possible to notice that in the latter range, the scaling is not necessary, as already pointed by Agathabay et al. [28] and Miranda et al. [29]. However, in benzimidazole L^2, this band was overlapped with the aromatic C=C bands in the same region under the effect of the intermolecular hydrogen bond. The theoretical value at 1684 cm^{-1} is assigned to υ(C=N). In Pt–L^1 complex (**2**), the υ(C=N) is shifted to lower frequency in comparable with that found in the uncoordinated ligand (Table 3). For Pt–L^2 complex (**4**), the C=N group is liberated from the effect of hydrogen bonding with increasing of double bond character and was observed at 1665 cm^{-1}. For Pd–$L^{1,2}$ complexes, this band is overlapped with the aromatic C=C bands in the same region and it is difficult to assign this vibration mode experimentally. The decrease of ν(NH) and ν(C=N) vibration modes in the imidazole ring indicated the participation of benzimidazole moiety in coordination sphere through the pyridine-type nitrogen.

The low-frequency vibrational data of the prepared complexes give an insight into the structure and bonding in the solid state. Unfortunately, the metal-nitrogen stretching bands could not be distinguished from other ring skeleton vibrations present in the same region [3]. However, the theoretical assignments of these bands are easily assigned by the visualization of the normal mode displacement vectors utilizing the *GAUSSVIEW* program as tabulated in Table 3. The far-IR spectra of Pd–$L^{1,2}$ complexes showed two medium bands at 369 and 363 cm^{-1}; which were absent in the free ligands; due to the ν(Pd—Cl) in a cis-square planar structure [24]. Similarly, the platinum complexes showed two bands at 372 and 360 cm^{-1} assign to the Pt—Cl bonds in cis-square-planar geometry [24]. The asymmetric and symmetric stretching modes as well as the scissoring bending mode of M—Cl bonds are presented in Table 3. The IR spectra of complexes **(1,2,4)** showed a very broad band centered at 3400 cm^{-1} associated by librational modes of water [30] as presented in Table 3.

Theoretically, the benzimidazoles $L^{1,2}$ give rise to eight C—H aromatic stretching mode of vibration corresponding to the presence of eight aromatic C—H bonds as shown in Tables 1 and 2. For assignments of CH_3 group frequencies theoretically, nine fundamentals can be associated to each CH_3 group [31], namely, CH_3^{ass}: asymmetric stretch (i.e. in-plane hydrogen stretching modes); CH_3^{ss}: symmetric stretch; CH_3^{ipb}: in-plane-bending (i.e. hydrogen deformation modes); CH_3^{sb}: symmetric bending; CH_3^{ipr}: in-plane rocking; CH_3^{opr}: out-of-plane rocking and τCH_3: twisting hydrogen bending modes. In addition to that, CH_3^{ops}: out-of-plane stretch and CH_3^{opb}: out-of-plane bending modes of the CH_3 group would be expected to be depolarized for A″ symmetry species. For L^1 derivative, the bands observed at 3033, 2956, and

Table 2
Band assignment of experimental and theoretical FT-IR spectra of benzimidazole L^2.

No	Exp. freq.	Calculated un-scaled frequency (B3LYP)		Scaled frequency uniform scaling		Scaled frequency linear regression scaling		Vibrational assignments
		6-31G(d)	LANL2DZ	6-31G(d)	LANL2DZ	6-31G(d)	LANL2DZ	
1		3649	3682	3514	3571	3499	3506	ν NH^{ss}/Bz
2	3434	3560	3615	3428	3506	3414	3442	ν NH^{ss}/An
3		3218	3238	3099	3140	3086	3083	ν CH^{ss}/Bz
4		3208	3224	3089	3127	3076	3070	ν CH^{ass}/Bz
5		3203	3214	3084	3117	3071	3060	ν CH^{ss}/An
6		3197	3209	3079	3112	3066	3056	ν CH^{ass}/Bz
7		3187	3196	3069	3100	3056	3043	ν CH^{ass}/Bz
8		3184	3198	3066	3102	3053	3045	ν CH^{ss}/An
9		3172	3180	3055	3084	3042	3028	ν CH^{ass}/An
10	3051	3166	3172	3049	3076	3036	3020	ν CH^{ass}/An
11		3116	3127	3001	3033	2988	2977	ν CH_3^{ass}
12		3083	3095	2969	3002	2956	2947	ν CH_3^{ass}
13	2908	3034	3027	2922	2936	2909	2882	ν CH_3^{ss}
14		3000	2979	2889	2889	2877	2837	CH_2^{ass}
15		2939	2960	2830	2871	2818	2818	CH_2^{ss}
16	1614	1684	1675	1622	1624	1614	1594	ν CC/An + ν CC/Bz + ν CN/Bz + β NH^{sc}/Bz
17			1678		1627		1597	ν CC/An
18		1642	1635	1581	1585	1574	1556	ν CC/Bz + β NH^{sc}/Bz
19		1635	1624	1575	1575	1567	1546	ν CC/An + β NH^{sc}/An
20		1595	1583	1536	1535	1529	1507	ν CC/Bz + β NH/Bz + β NH/An + $\delta_s CH_2$ + ν C=N/Bz
21	1519	1576	1568	1518	1520	1511	1492	ν CC/An + β NH/An + $\delta_s CH_2$
22		1547		1581		1479		$\beta NH/An + CH_3^{opb}$
23		1543	1538	1486	1491	1479	1464	$\delta_s CH_2$
24		1535		1478		1471		$\delta_s CH_2$ + ν C—N/Bz + ν CC/An
25		1523	1533	1467	1487	1460	1459	$\beta NH/An + CH_3^{opb}$
			1517		1471		1444	
26		1515	1516	1459	1470	1452	1443	CH_3^{ipb}
27		1497	1480	1442	1435	1435	1408	ν CC/Bz (boat shape)
28	1421	1471		1417		1410		ν CC/An + β CH/An + β CH/Bz + ν C—NH/Bz + ωCH_2
29		1453	1454	1399	1410	1393	1384	$CH_3^{sb} + \omega CH_2 + \beta CH/An$
30		1445	1446	1392	1402	1385	1376	CH_3^{sb}
31		1425	1434	1372	1390	1366	1365	ν CC/Bz + ωCH_2 + β NH/Bz + β NH/An + β CH/Bz
32			1382		1340		1315	ν CC/An + β NH/An
33	1306	1355	1360	1305	1319	1299	1294	β CH/An
34		1332	1325	1283	1285	1277	1261	β $CH^{ss,sc}$/Bz + β $CH^{ss,sc}$/An + β NH/An + ωCH_2
35	1264		1290		1251		1227	β CH/Bz + β NH/An
36			1250		1212		1189	ν CCH_3/An
37	1226	1259		1212		1207		τCH_2 + β CH/Bz + β NH/Bz
38		1247	1248	1201	1210	1195	1187	τCH_2
39		1244		1198		1192		ν CCH_3/An + β CH/An
40		1221		1176		1170		β $CH^{ss,sc}$/An
41		1207	1224	1162	1187	1157	1165	β CH/An + β CH/Bz + β NH/Bz
42			1229		1192		1169	β NH/Bz + β$CH^{ss,sc}$/An
			1223		1186		1164	
43		1183	1193	1139	1157	1134	1135	β $CH^{ss,sc}$/Bz
44	1121	1166	1170	1123	1134	1118	1113	ν CH_2—NH/An + β$CH^{ss,sc}$/An
45		1144	1169	1102	1133	1096	1112	ν CH_2—NH/An + β $CH^{ss,sc}$/An + β $CH^{ss,sc}$/Bz
			1145		1110		1089	
46			1139		1104		1084	β $CH^{ss,sc}$/Bz
47		1076	1084	1036	1051	1031	1031	CH_3^{opr}
48			1035		1003		985	Rtorsion/Bz
49		1032	1031	994	1000	989	981	Rtorsion/An + ρCH_2
50		1039	1050	1001	1018	996	999	ρCH_2
		674	675	649	654	646	642	
51			1008		977		959	Rtorsion/Bz
52		1016	1015	978	984	974	966	CH_3^{ipr}
53	742	974	1024	938	993	933	974	γ CH/Bz
		930	982	896	952	891	934	
		861	896	829	869	825	852	
		776	786	747	762	743	747	
		757		729		725		
		589		567		564		
	899	946	997	911	967	906	948	γ CH/An
54	806	932	852	897	826	893	810	
		827	840	796	814	792	799	
		814		784		780		
55		912	908	878	880	874	864	Rtrigd/Bz
56		885	873	852	846.	848	830	Rtorsion/An
57		789	782	760	758	756	744	Para deformation of aniline ring
58		659	660	635	640	631	627	Rtrigd/An

Table 2 (*continued*)

No	Exp. freq.	Calculated un-scaled frequency (B3LYP)		Scaled frequency uniform scaling		Scaled frequency linear regression scaling		Vibrational assignments
		6-31G(d)	LANL2DZ	6-31G(d)	LANL2DZ	6-31G(d)	LANL2DZ	
59		631	635	608	615	604	603	Rtrigd/Bz
60	586	597	522	575	506	572	496	NH/An
61		589	595	567	577	564	565	NH/Bz
62		323	337	311	326	309	320	τCH_3

For 6-31G(d) basis set, the slope is equal 1.0425 and the linear coefficient is 0.9997.
For LANL2DZ basis set, the slope is equal 1.0497 and the linear coefficient is 0.998.

Table 3
IR band assignment of Pd(II) and Pt(II) complexes with benzimidazoles $L^{1,2}$ calculated at the B3LYP/LANL2DZ.

Calculated/(observed)				Band assignment
$[PdL^1Cl_2]\cdot 3H_2O$	$[PtL^1Cl_2]\cdot H_2O$	$[PdL^2Cl_2]$	$[PtL^2Cl_2]\cdot 2H_2O$	
3571	3572 (3225)	3572 (3227)	3573 (3243)	ν NH^{ss}/Bz
3375 (3433)	3361 (3427)	3376 (3411)	3357 (3430)	ν NH^{ss}/An
1593 (1444)	1595 (1449)	1595 (1446)	1597 (1451)	ν CC/An + β NH^{sc}/An
1587	1588	1588	1588	ν CC/Bz + β NH^{sc}/Bz
1524	1526 (1636)	1524	1526 (1665)	ν C=N/Bz
1430	1440 (1332)	1429	1441 (1384)	ν C—N/Bz
1249	1183	1183 (1281)	1183 (1284)	ν C—N/An
629	631	631	631	ν M—N_{py}
586	568	586	570	γ NH/Bz
478	536	466	531	ν M—NH_{sec}
333		274		ν M—Cl23 trans to NH_{sec}
324	323	276		ν M—Cl22 trans to N_{py}
304	320	331	323	ν Cl—M—Cl^{ss}
285	314	322	317	ν Cl—M—Cl^{ass}
126	113	127	114	β Cl—M—Cl^{sc}
(658w $\rho_w(OH_2)$, 527w $\rho_t(OH_2)$)	(533w $\rho_t(OH_2)$)		(697w $\rho_w(OH_2)$, 525w $\rho_t(OH_2)$)	Librational modes of water

Bz: benzimidazole, sec: secondary amino group, py: pyridine, others below Table 1.

2903 cm^{-1} are ascribed to CH_3 asymmetric and symmetric stretching vibration as calculated using the basis set 6-31G(d). Infrared bands established at 1480, 1464, 1446, 1173, 1143 and 249 cm^{-1} are attributed to CH_3^{opb}, CH_3^{ipb}, CH_3^{sb}, CH_3^{opr}, CH_3^{ipr}, and τCH_3 vibration mode, respectively. For benzimidazole (L^2), the IR bands observed at 3001, 2969; 2922, 1467, 1459, 1392, 1036, 978 and 311 cm^{-1} are unambiguously assigned to CH_3^{ass}; CH_3^{ss}, CH_3^{opb}, CH_3^{ipb}, CH_3^{sb}, CH_3^{opr}, CH_3^{ipr}, and τCH_3 vibration mode, respectively. Other vibration modes are shown in Tables 1 and 2.

Any discrepancy noted between the observed and the calculated frequencies may be justified on the basis that the theoretical calculations were carried out on a single molecule in the gaseous state contrary to the experimental values recorded in the presence of intermolecular interactions. The difference in vibrational frequencies calculated by the two different basis sets may be partially explained by the electron-correlation effect. The RMS error of the frequencies between the un-scaled and experimentally observed in case of benzimidazole L^2 for example was found to be 73 cm^{-1}. After scaling, the RMS error are found to be 8 and 25 cm^{-1} for 6-31G(d) and LANL2DZ basis sets, respectively, suggesting that the 6-31G(d) basis set gives more accurate results which is in agreement with the previously reported work [28,29].

3.2. ^1H NMR studies

The theoretical prediction of NMR shieldings is important in the characterization of molecular electronic structure. Calculations of magnetic properties inherently suffer from a "*gauge origin*" problem, which simply means that the results depend on the choice of the origin of the coordinate system. This clearly non-physical behavior can be avoided by assigning a local gauge origin to each basis function, which is known as a "*gauge-independent atomic orbital*" (GIAO) [15]. In the present study, the ^1H NMR calculations were performed using GIAO method using 6-311 + G(2d,p) and LANL2DZ basis sets. The ^1H shielding was converted into the predicted chemical shifts using δH-TMS values 31.88 and 32.77 ppm for 6-311 + G(2d,p) and LANL2DZ basis sets, respectively. The experimental and theoretical ^1H-chemical shifts δ(ppm) of the benzimidazoles and their complexes are presented in Table 4.

The spectral assignments of the complexes were based on comparison with the shapes and positions in the corresponding spectrum of the uncoordinated ligand. A comparison indicated a positive coordination-induced shift (c.i.s. = $\delta_{complex} - \delta_{ligand}$), implying that decomposition has not occurred in solution [32] and there is a considerable deshielding effect upon coordination. Almost all signals are shifted upon complexation, as a result of the electric field effect caused by complexation, π-bonding and temperature-independent paramagnetism of the palladium and platinum metal ion [32].

The ligands $L^{1,2}$ showed broad singlet signals at 12.23 and 12.21 ppm [33], respectively, due to the benzimidazolic NH proton. The large downfield shift of this proton may be attributed to the presence of intermolecular hydrogen bond as previously mentioned. In complexes, this proton is observed at 13.14 ppm for Pd–$L^{1,2}$ and 13.29 and 13.35 ppm for Pt–$L^{1,2}$, respectively, which can be related to the charge density change in the benzimidazole ring supporting that coordination occurs *via* the pyridine-type nitrogen and causing inhibition of the fluxional behavior of the imine ring [34]. The protons of the CH_2 groups in benzimidazoles $L^{1,2}$ are deshielded by the presence of the secondary amino group

Table 4
The experimental and theoretical ^{1}H NMR chemical shifts δ (ppm) from TMS for the studied compounds.

L^1			$Pd–L^1$		$Pt–L^1$		L^2			$Pd–L^2$		$Pt–L^2$		Assignment
Exp.	Calcd (a)	Calcd (b)	Exp.	Calcd (b)	Exp.	Calcd (b)	Exp.	Calcd (a)	Calcd (b)	Exp.	Calcd (b)	Exp.	Calcd (b)	
12.23	8.13	7.50	13.14	11.17	13.29	9.86	12.21	8.13	7.50	13.14	11.16	13.35	9.87	(1H), Benzimidazolic NH
6.89	7.08	7.34		6.83		6.38	6.88	7.48	7.48		6.62		6.76	(4H), aniline ring protons
6.86	7.06	6.96		6.75		5.71	6.85	7.19	7.25		6.08		5.90	
6.57	6.98	6.69		5.23		5.66	6.56	7.14	7.08		5.17		5.66	
6.55	6.49	6.47	6.28–8.80	5.22	6.54–8.57	5.56	6.53	6.25	6.37	6.44–8.60	5.16	6.34–8.09	5.56	
7.52	8.13	8.11		8.26		8.72	7.51	8.14	8.13		8.17		8.72	(4H), Benzimidazole ring protons
7.47	7.61	7.66		8.25		8.02	7.46	7.61	7.67		7.98		8.02	
7.12	7.57	7.59		7.59		7.31	7.13	7.58	7.60				7.31	
7.10	7.55	7.40		6.86		7.14	7.09	7.56	7.40		7.66 7.42		7.13	
5.80	5.16	5.29		3.79	7.07	6.86	6.00	5.36	5.42	7.46	4.00		6.85	(1H), secondary amino proton
4.41	4.40	4.12	5.00	4.29	4.75	4.61	4.42	4.41	4.07	4.93	4.27	4.70	4.63	(2H), CH_2
				3.77	5.06	3.12				5.27	3.84	4.92	3.10	
3.61	3.78	3.55	3.75	1.93	3.72	2.45	2.10	2.32	2.29	2.14	0.87	2.13	0.47	(3H), CH_3

(a) 6-311+(2d,p) (b) LANL2DZ.

Table 5
Kinetic parameters (E^*, ΔH^*, ΔG^*; kJ/mol), A (s^{-1}) and ΔS^* (J/K mol); determined using Coats–Redfern method and Horowitz–Metzger methods of the metal complexes under study PtL^1 and PdL^2 (selected).

Compound	Decomp. range	Coats–Redfern					Horowitz–Metzger				
		E^*	A	ΔS^*	ΔH^*	ΔG^*	E^*	A	ΔS^*	ΔH^*	ΔG^*
$[PtL^1Cl_2]\cdot H_2O$	31–97	25	1×10^5	−148	22	73	25	1×10^5	−148	22	73
	97–394	19	2×10^5	−149	15	96	22	1×10^6	−132	17	91
	394–500	119	4×10^5	−145	113	213	112	2×10^5	−151	106	210
$[PdL^2Cl_2]$	225–340	92	2×10^5	−150	87	169	90	2×10^5	−151	85	169
	340–507	230	4×10^7	−106	224	295	247	1×10^8	−95	241	305

with appearance of doublet signal at 4.41 ppm. This signal shifts to higher frequencies in the studied complexes, indicates that the secondary amino group is also coordinated to the metal centre. As shown in Table 4, the methylene resonance appears as a pair of quartet at 4.70–5.27 ppm for all the studied complexes. A quartet would be expected due to that the methylene CH_2 geminal protons are no longer isochronous. This can be attributed to differences in polarization of the C—H bonds between the axial and equatorial CH_2 protons in the complexes. This polarization; enhanced in DMSO; results in a deshielding of the equatorial protons, which point away from the metal ion [35]. Benzimidazoles ($L^{1,2}$) displayed additional singlet signals at δ 3.60 and 2.10 ppm, with integration corresponding to three protons of the substituents, methoxyl and methyl groups in the aromatic ring, respectively.

Ligands $L^{1,2}$ exhibited signals for the secondary amino NH protons at 5.80 and 6.00 ppm, respectively, that obscured by the aromatic signals and disappear on deuteration. This proton is deshielded due to the anisotropy of the ring and the resonance that removes electron density from nitrogen and changes its hybridization. In complexes, this proton moves downfield with respect to its position in the free ligands as a result of the participation of the NH_{sec} group in the coordination sphere and still obscured by the aromatic protons (Fig. 2). The calculations from the integration curves of aromatic signals indicated the presence of eight protons ascribes to the aromatic protons and one proton is suggested to the proton of NH_{sec} group.

The multi-signals of the aromatic protons appear as a complex signal at δ = 6.55–7.52 ppm in benzimidazoles $L^{1,2}$. For benzimidazole L^1, the protons of the aniline ring give rise to four-line pattern at 6.55 and 6.57 ppm for protons in the ortho-position with respect to secondary amino group whereas the protons at 6.86 and 6.89 ppm are assigned to aromatic protons in the ortho-position with respect to methoxyl group. In addition, the benzimidazole protons are much broader due to the expected cross-ring couplings, which are characteristic of such systems [36] at 7.10, 7.12, 7.47 and 7.52 ppm. Similar, L^2 has the same assignments for the aromatic protons as L^1 at 6.53, 6.56, 6.85, 6.88 and 7.09, 7.13, 7.46, 7.51, respectively. In the metal complexes, the aromatic protons nearest the pyridine-type nitrogen and the secondary amino group were found to suffer maximum downfield shifts in comparison with the other aromatic protons confirming that ligands $L^{1,2}$ interact with metal ions through the pyridine like nitrogen and secondary amino group.

The calculated chemical shifts of the methylene, methyl, and methoxyl groups in the studied benzimidazoles ($L^{1,2}$) using 6-311 + G(2d,p) and LANL2DZ basis sets are in a good agreement with the experimental values as shown in Table 4. However, the experimental chemical shifts of the other protons in the benzimidazoles are slightly smaller than the calculated values and the largest deviations are observed in the low field of the spectra. The experimental chemical shift of the benzimidazolic NH proton is shifted towards higher magnetic field than the calculated ones by about 4 ppm, as previously reported by other authors [37]. This may be due to neglect of the non-specific solute–solvent interactions (in the gas phase), and the intermolecular hydrogen bond in our calculations as compared with the experimental chemical shifts that are obtained from the DMSO solutions (hydrogen-bonded solvent). The NH protons form hydrogen bond with DMSO molecules and move downfield. GIAO method showed significant difference in chemical shifts between the hydrogen-bonding protons and non-hydrogen-bonding protons [37]. These differences were 3.02 in the gaseous phase, 1.17 in DMSO, and 1.22 ppm in

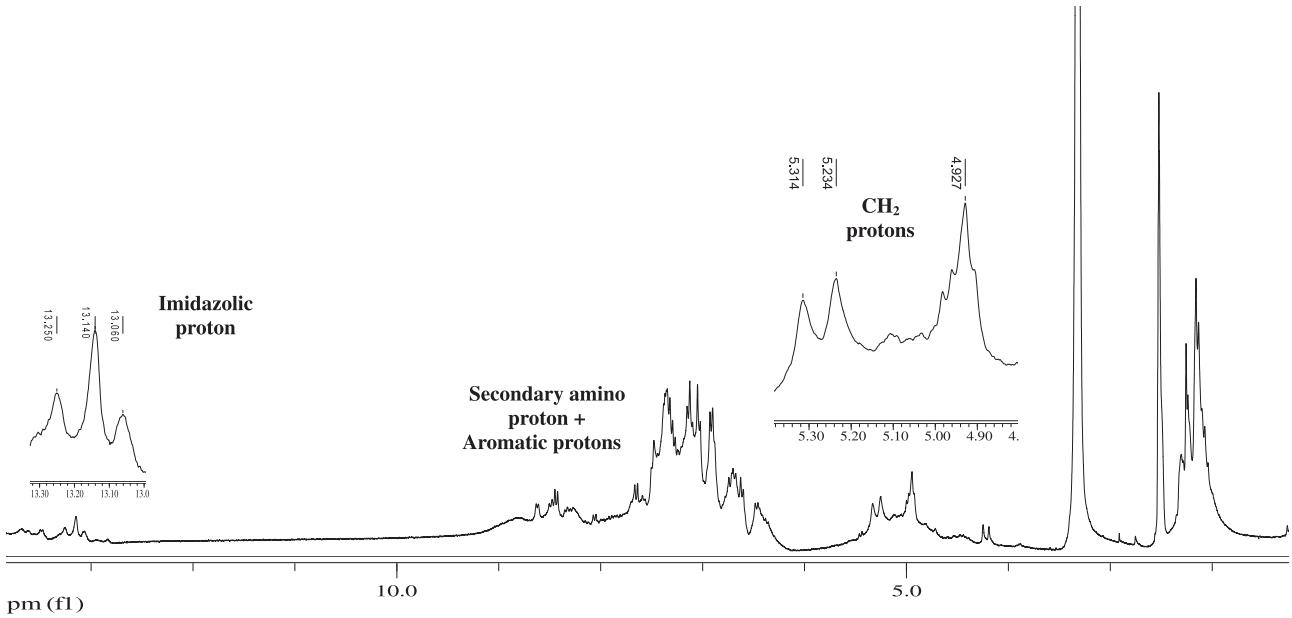

Fig. 2. ^{1}H NMR spectra of Pd–L^2 complex in DMSO.

the aqueous phase as discussed by Miranda et al. [29]. The calculated chemical shifts for non inter- or intramolecular hydrogen-bonding protons are far from the experimental values and the inclusion of solvent is necessary in order to increase the chemical shift by 1.50 ppm (in case of DMSO); as discussed by several authors [29]; which shows the importance of the use of solvation in shielding calculations.

3.3. Mass spectrometry

The electron impact mass spectra of the ligands L^{1,2} and their complexes were recorded and investigated at 70 eV. The benzimidazoles (L^{1,2}) have strong molecular ion peaks (M$^+$) at *m*/*z* 253 and 237, respectively. These compounds undergo fragmentation through cleavage of CH_2—NH bond with the appearance of a fragment at *m*/*z* 131; which assign to 2-methylene benzimidazole fragment; and fragments at *m*/*z* 123 and 107 due to the formation of para-anisidine and para-toluidine fragments, respectively. The fragment at *m*/*z* 118 is assigned to the benzimidazole ring. For benzimidazole L^2, further fragmentation occurs by the elimination of NH_{sec} group from the most predominant fragment (para-toluidine) forming a benzyl cation, which spontaneously rearranges to form a tropylium ion. However, L^1 derivative shows a fragment at *m*/*z* 238 due to the loss of methyl group from M$^+$, followed by the removal of CO and one ionizable proton to give a peak at *m*/*z* 209.

The mass spectrum of Pd(II)–L^1 shows three fragmentation routes as shown in Scheme 1. The first route represents the loss of methoxyl group to provide a peak at *m*/*z* 399; [Pd(L^1—OCH_3)Cl_2]; followed by the removal of one chlorine atom to give the most abundant peak at *m*/*z* 365; [Pd(L^1—OCH_3)Cl]. The latter fragment eliminates the imidazolic NH group to offer a fragment at *m*/*z* 350;[Pd(L^1—OCH_3—NH)Cl]$^+$. The 2nd dissociation process involves the loss of CH_3 group and one chlorine atom to supply a peak at *m*/*z* 381, [Pd(L^1—CH_3)Cl]. The 3rd stage represents the elimination of benzimidazole ring, and two chlorine atoms to give peak at *m*/*z* 243, followed by the dissociation of methoxyl group to afford a peak at *m*/*z* 211. Several observed fragments confirmed the bidentate nature of the ligand L^1 were observed.

The mass spectrum of Pt–L^1 complex has a weak molecular ion peak at *m*/*z* 516 corresponding to M-2; (M = [Pt(L^1)Cl_2]$^+$); followed by the removal of methoxyl group, two chlorine atoms and two acetylene groups from the benzimidazole ring to give a fragment at *m*/*z* 365. Thus, the participation of the pyridine-type nitrogen in the coordination sphere withdraws the electron density from the benzimidazole ring and introduces a second weakness point through which the fragmentation can proceed with degradation of benzimidazole ring to imidazole moiety. The latter fragment eliminates the imidazolic NH group to offer a fragment at *m*/*z* 350.

The fragmentation pattern of Pd–L^2 complex resembles that of Pd–L^1 with two decomposition routes. The first step results in the formation of fragments at *m*/*z* 365 and 350 as found in Pd–L^1 complex. The 2nd route involves either the loss of one chlorine atom and p-toluidine moiety to give a peak at *m*/*z* 258, [Pd(benzimidazole)Cl]$^+$ or benzimidazole ring to give a fragment at *m*/*z* 295. These two fragments confirmed the bidentate nature of this ligand. For Pt–L^2 complex, the fragment at *m*/*z* 450 is due to the dissociation of methyl group and one chlorine atom from M$^+$. In addition, this complex shows the same fragments at *m*/*z* 365 and 350 as previously found in Pt–L^1.

3.4. Electronic absorption

The electronic spectra of L^{1,2} displayed five absorption bands in ethanol. The first band at 204 nm may be assigned to the medium energy π—π^* transition within the phenyl rings of the aniline and benzimidazole moieties [38]; (^1L_a—^1A). While the second band at 223 (L^1) and 222 (L^2) nm is attributed to the low energy π—π^* electronic transition of the phenyl rings of both the aniline and benzimidazole moieties (^1L_b—^1A) [38]. In the benzimidazole ring, three kinds of transitions are possible: (i) n—π^*, (ii) π—π^*, and (iii) charge-transfer (CT). The nature of the transition depends upon the type of solvent used and the nature of the substituents [39]. It is well established that the n—π^* transition is not observed in the benzimidazole compounds, although the system has a lone pair of electrons on the tertiary nitrogen atom [39,40]. Distinction between π—π^* and charge-transfer bands can be made from the study of the effects of solvents on the absorption spectra and changing of the substituent (nature and position) on the benzene ring [38]. Therefore, the remaining bands at 242, 273 (L^1) or 274 (L^2) and 280 nm may be assigned to π—π^* transitions in the delocalized

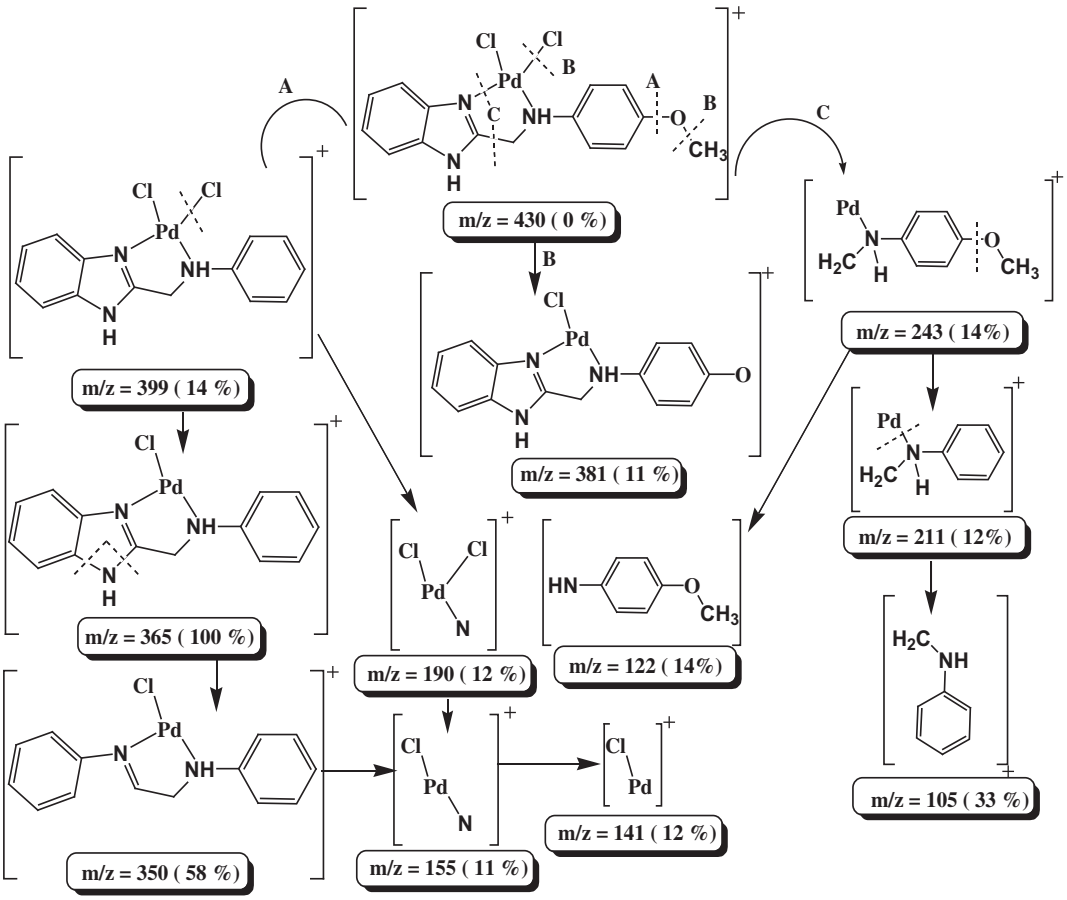

Scheme 1. Fragmentation pattern of Pd–L[1] complex.

π-electron system and in the heteroatomic groups inside the benzimidazole molecule [41]. The latter two bands; 273 (or 274) and 280 nm appear doubled like benzoic acid due to probable existence of a tautomeric structure [42]. This phenomenon is supported by comparing our spectra with the spectrum of 1-methyl-2-phenylbenzimidazole [39], where this fine structure is lost. On comparing the absorption spectra of L with the parent 2-methylbenzimidazole (280, 274 nm, L_b; 245 nm, L_a) [39], it can be concluded that the two normal band systems are kept nearly intact except that L_a transition is slightly blue shifted.

The electronic spectra of 10^{-4} M of the studied complexes were scanned in DMF as shown in Fig. 3. The two bands between 270 and 280 nm (35714–37000 cm^{-1}) in Pd–$L^{1,2}$ and Pt–$L^{1,2}$ complexes are assigned to the internal ligand transitions (π—π^* transitions in the benzimidazole ring). Both, the π—π^* transitions in the ligand and the cutoff of the solvent prevent the observation of LMCT in the UV region. By assuming a value of $F_2 = 10F_4 = 600$ cm^{-1} for a Slater–Condon interelectronic repulsion parameters [43], it is possible to derive the values of Δ_1; $\Delta_1 = \nu_1 + 3.5F_2$; from the first spin allowed d-d transition. The first low energy spin allowed bands at 22,831 ($\Delta_1 = 24{,}931$ cm^{-1}, $\log \varepsilon_{max} = 3.66$) and 23,696 cm^{-1} ($\Delta_1 = 25{,}796$ cm^{-1}, $\log \varepsilon_{max} = 364$) in Pt–$L^{1,2}$ complexes, respectively, have been assigned to the transition $b_{2g}(d_{xy}) - d_{1g}(d_{x^2-y^2})$, i.e. $^1A_{1g} \rightarrow {}^1A_{2g}$ (ν_1). While, the band at 26,385 cm^{-1} ($\log \varepsilon_{max} = 3.55$) in Pt–$L^1$ complex is spin-allowed transition; $a_{1g}(d_{x^2-y^2}) - b_{1g}(d_{x^2-y^2})$, i.e. $^1A_{1g} \rightarrow {}^1B_{1g}$ (ν_2). Strong charge-transfer transitions may interfere and prevent observation of all the expected bands [44]. However, strong bands between 350 and 380 nm (28,000–26,500 cm^{-1}) are assignable to a combination of MLCT and $e_g(d_{yz', dzx}) - b_{1g}(d_{x^2-y^2})$ i.e. $^1A_{1g} \rightarrow {}^1E_g$ bands (ν_3). Thus, the bands located at 27,700 ($\log \varepsilon_{max} = 3.48$), 27,472 ($\log \varepsilon_{max} = 3.59$) and 27,247 cm^{-1} ($\log \varepsilon_{max} = 3.25$) in Pt–$L^2$ and Pd–$L^{1,2}$ complexes, respectively, are assigned to this combination. Therefore, the electronic spectra of Pd–$L^{1,2}$ and Pt–$L^{1,2}$ metal complexes are indicative of square-planar geometry [44].

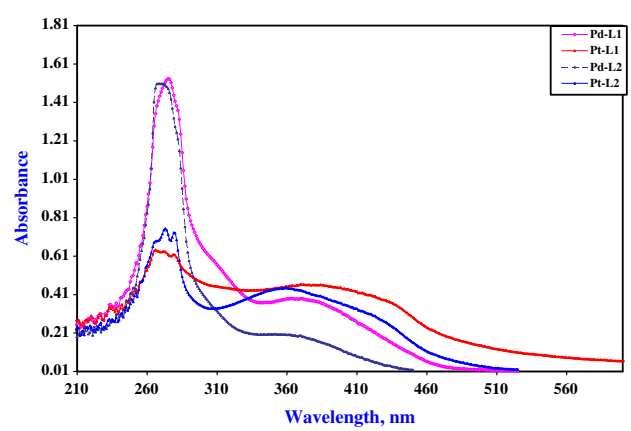

Fig. 3. Electronic absorption spectra of 10^{-4} M solutions of Pd–$L^{1,2}$ and Pt–$L^{1,2}$ complexes in DMF.

3.5. Molar conductance measurements

The molar conductance values of 10^{-3} M for Pd–$L^{1,2}$ and Pt–$L^{1,2}$ complexes in DMF revealed low conductance values 9.68, 17.42, 8.02 and 8.63 ohm^{-1} cm^2 $mole^{-1}$, respectively, this may be taken

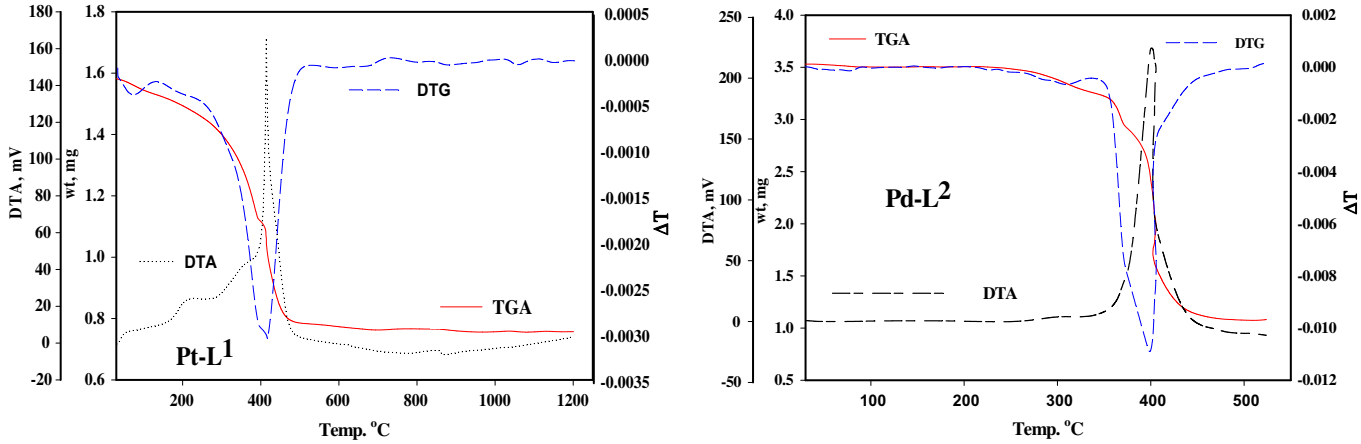

Fig. 4. TGA, DTG and DTA curves of Pt–L^1, and Pd–L^2.

as an evidence for the presence of chlorine atoms inside the coordination sphere of these complexes, indicating the non electrolytic nature of these complexes.

3.6. Thermal analyses and kinetics studies

The simultaneous TGA-DTA curves for Pd–L^1complex **(1)** exhibit three distinct decomposition stages maximized at 330, 395 and 817 °C. The first pronounced peak is accompanied by a mass loss, which amounts to 25.94%. This value finds a parallelism with the calculated value (25.80%) responsible for desorption of three water molecules of hydration and chlorine gas. The 2nd and 3rd thermal stages, bring the total mass loss up to 77.94% (calcd. 78.02%) of the parent complex with degradation of one ligand molecule leaving Pd metal as a final residue. It is clear from DTA curve that these mass losses are accompanied by two endothermic peaks at 330 and 395 °C and one exothermic peak at 817 °C. The powder X-ray diffraction pattern of the residue of Pd–L^1 complex was recorded directly after TGA and the results were compared with those that are available at the international center for the diffraction data. The XRD pattern shows major diffraction peaks at $2\theta = 40.1$ (1 1 1) and 46.7 (2 0 0) as previously reported for the palladium metal. In addition, the residue of the Pd–L^1 complex exhibited metallic luster confirming its metallic nature.

For Pd–L^2 complex **(3)**, the degradation starts at 225 °C, with two endothermic peaks maximized at 280 and 399 °C as shown in Fig. 4. The 1st stage reveals the elimination of one chlorine atom with mass loss amounts to 8.50% (calcd. 8.45%), while the 2nd decomposition step is corresponding to the loss of one ligand molecule and another chlorine atom leaving Pd + C as a final residue. This statement is in accordance with the results obtained for other Pd(II) and Pt(II) complexes [45]. This behavior confirms that the two chlorine atoms are not isoenergetically bound and thus their elimination takes place via two different overlapping steps [46].

Examining the simultaneous TGA-DTA curves constructed for Pt–L^1 complex **(2)**, Fig. 4, one can observe three mass loss stages maximized at 73, 280 and 414 °C. The first two endothermic decomposition steps are responsible for desorption of one physically adsorbed water molecule, one chlorine atom and benzimidazole ring with a mass loss 30.89% (calcd. 30.81%). The 3rd endo-thermic stage is accompanied by a mass loss of 29.46% (calcd. 29.46%) responsible for degradation of the rest of the organic part and another chlorine atom leaving Pt + C as a final residue.

Degradation of Pt–L^2 complex **(4)** is incomplete up to 1200 °C with two endothermic peaks at 280 and 414 °C; like Pt–L^1; in nitrogen atmosphere. The overall mass loss amounts to 52.75% (calcd. 63.82%) assuming that the thermal decomposition process proceeds with the formation of Pt metal, as final residue as no other platinum compounds are present over 1200 ° C. This behavior [47] reflects the high stability of this complex in comparable with Pt–L^1 complex. The rate of decomposition of most complexes is fast in air than that in nitrogen [48]. Although the masses losses in air in most metal complexes, [49] start at comparatively high temperatures, complete thermal degradation is achieved at lower temperatures than in nitrogen. This change in temperature seems to be due to the oxidative nature of air, which facilitates the oxidative decomposition [48,49]. In air, this complex shows two degradation steps with overall mass loss 63.61%.

There has been increasing interest in determining rate-dependent parameters of solid-state non-isothermal decomposition reactions by analysis of TGA curves. Several equations [50–52] have been proposed to analyze TGA curves and obtain values for kinetic parameters. The kinetics parameters are calculated by using Coats–Redfern [50] and Horowitz–Metzger methods [51] (Table 5). According to the thermodynamic data obtained from the TGA curves, it was found that the metal complexes have negative entropy, which indicates that the complexes are formed spontaneously and are highly ordered in their activated states. For $[PdL^2Cl_2]$ complex, the activation energy values increases on going from one decomposition stage to another for a given complex, indicating that the rate of decomposition decreases in the same order. The values of the free activation energy ΔG^* increases significantly for the subsequent decomposition stages of a given complex. This is due to increasing the values of $T\Delta S^*$ significantly from one-step to another which override the values of ΔH^*. This may be attributed to the structural rigidity of the remaining part of the complex after the expulsion of one of the coordinated anions or water molecules, as compared with the precedent complex, which require more energy, $T\Delta S^*$ for its rearrangement before undergoing any structural change. The positive ΔH^* values mean that the decomposition processes are endothermic.

3.7. X-ray powder diffraction

Single crystals of the studied complexes could not be obtained, because the studied complexes are amorphous in their nature, in addition to their insolubility in most organic solvents except DMF and DMSO. The X-ray powder diffraction patterns of the benzimidazole L^2 and its Pd(II) and Pt(II) complexes as representative examples were recorded over $2\theta = 5–60°$ in order to obtain an idea about the lattice dynamics of these compounds. The comparison between the obtained XRD patterns of L^2 and its complexes (Fig. 5), throw light on the fact that each complex represents a definite compound with a distinct structure. This identification of the

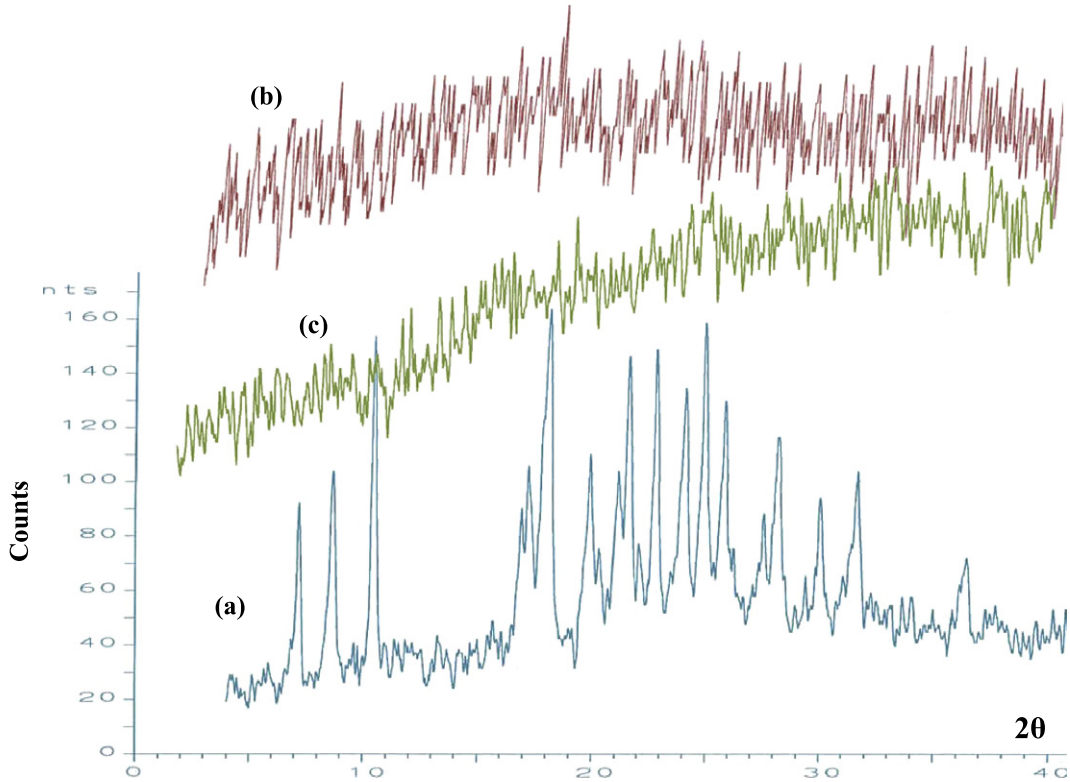

Fig. 5. X-ray diffraction pattern of (a) benzimidazole L^2, (b) Pd–L^2 and (c) Pt–L^2.

Table 6
X-ray diffraction data of benzimidazole L^2.

Angle (2θ)	*d*-Value (Å)	Relative intensity ($I/I°$)%
7.21	12.25	55.6
8.71	10.14	56.9
10.49	8.42	100
17.27	5.13	51.6
18.16	4.87	96.4
19.92	4.45	54.2
21.15	4.19	50.3
21.59	4.11	86.0
22.80	3.89	87.7
24.08	3.69	73
24.93	3.56	92.9
25.84	3.44	76.2
28.20	3.16	59.7
30.05	2.97	38.2
31.69	2.82	46.5
36.36	2.46	20.7
44.01	2.06	4.4

complexes was done by the known method [53]. Such facts suggest that the prepared complexes are amorphous. The X-ray powder diffraction pattern of benzimidazole (L^2) showed a higher degree of crystallinity as the parent benzimidazole [54]. The values of 2θ, interplanar spacing d (Å) and the relative intensities ($I/I°$) of benzimidazole L^2 were tabulated in Table 6. The data from this pattern show three low-angle diffraction peaks (below 10.5°) that are not observed in the parent benzimidazole with acceptable intensity. Several peaks characterized to the benzimidazole moiety are also observed at 17.27°, 18.17°, 19.92°, 31.69°, and 36.36°.

3.8. Theoretical calculations

Full geometry optimizations were performed at the DFT level of theory [13]. The optimized bond lengths of C=N and C—NH in the benzimidazole ring of compounds $L^{1,2}$ are 1.310 and 1.377 Å for B3LYP/6-31G(d) as shown in Tables 7 and 8. This discrepancy between the C=N and C—NH bond lengths confirm that the hydrogen atom is fixed at one of the two nitrogen atoms through the previously mentioned intermolecular hydrogen bond. These values are coincided with those found from the optimization of benzimidazole and 2-methylbenzimidazole [55] under the same level of theory. In addition, these latter bonds have a shorter distance than any amine compound, which is due to the participation of the lone electron pair of nitrogen atom in resonance of benzimidazole rings [55]. The most optimized geometry in L^2 derivative reveals that, the methyl group is in antiform, i.e. the hydrogen atoms in the plane are in the anti-position with respect to the aniline ring. Because of the increased conjugation effect, there is strengthening (and shortening) of the aryl-O bond C31—O30. These benzimidazole compounds show accumulation of the negative charge density on the pyridine-type nitrogen in the imidazole ring as shown in Tables 7 and 8 and this negative charge facilitates intermolecular hydrogen bonding, which is a very important structural feature related directly to the ability to bind the metal ions. Several calculated thermodynamic parameters are presented in Tables 7 and 8. The dipole moment increases dramatically from a value of 2.296 D (L^1 derivative) to 3.386 D (L^2 derivative), where the high electronegativity of CH_3 group induces strong polarization both in σ- and π-frameworks of the aniline moiety than the OCH_3 group.

The fully optimized geometries of cis-Pd$L^{1,2}Cl_2$ and cis-Pt$L^{1,2}Cl_2$ and numbering of atoms are shown in Fig. 6. Some selected geometric parameters as calculated by B3LYP/LANL2DZ are listed in Tables 9 and 10. According to the theoretical calculations, the lowest energy structures of these complexes are of C_1 symmetry. The Pd(II) and Pt(II) ions are in square-planar geometry, in which the metal ion is coordinated to a bidentate ligand through the pyridine-type nitrogen of imidazole ring and the secondary amino group, providing a five-membered chelate ring as well as two chlorine atoms. The optimized structures of cis-PdL^2Cl_2 **(2)** and

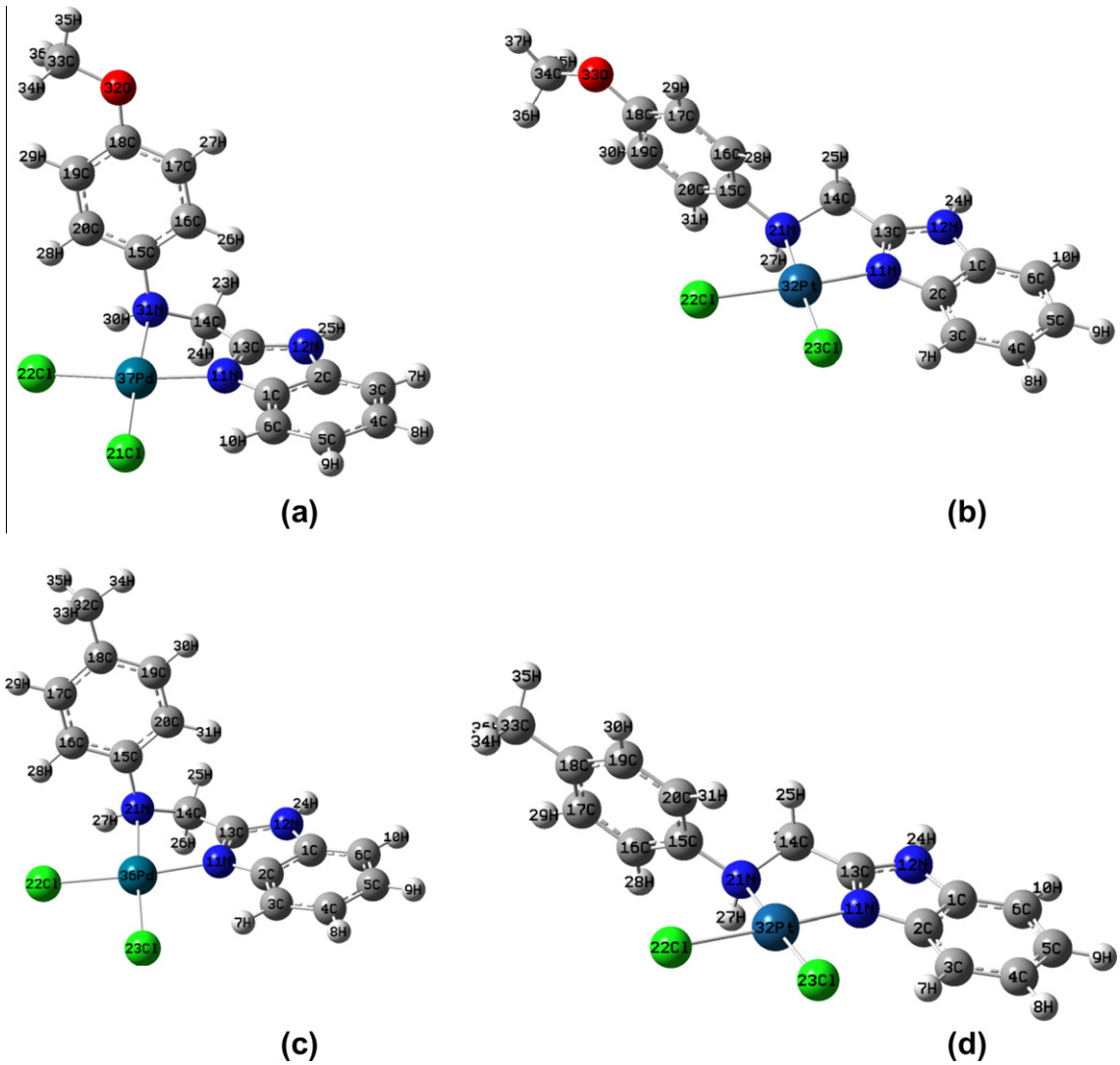

Fig. 6. The optimized structures of (a) Pd–L^1 (b) Pt–L^1 (c) Pd–L^2 (d) Pt–L^2 complexes.

cis-PtL^2Cl_2 **(4)** will be discussed in details as examples for the studied complexes. As shown in Fig. 6, the four donor atoms (N, NH, 2Cl) are coplanar, while the phenyl group of the aniline ring is bent out of the plane by angle 89.349° and 158.500° for cis-PdL^2Cl_2 and cis-PtL^2Cl_2 complexes, respectively. The calculated geometrical parameters (bond lengths and angles) are comparable to the experimental data of cis-platin.

The M-nitrogen bonds (M = Pd or Pt) are of comparable lengths, the M—NH_{sec} (NH_{sec} = secondary amino nitrogen) distance is only about 4.43% longer than that of M—N_{py} (N_{py} = pyridine-like nitrogen) bond distance (Tables 9 and 10) [56]. It is seen that the optimized M—NH_{sec} and M—N_{py} bond lengths in Pd–L^2 complex are slightly larger than the corresponding Pt—NH_3 in cis-platin by 0.16 and 0.06 Å, respectively, while the M—Cl bond lengths are larger by 0.06 and 0.04 Å for M—Cl22 and M—Cl23, respectively, owing to the trans-effect. For cis-PtL^2Cl_2 **(4)** complex, the M—N_{py} and M—NH_{sec} bond distances are shorter than the corresponding one in cis-PdL^2Cl_2 **(2)** complex by 0.017 Å.

For cis-PdL^2Cl_2 complex, the optimized N11—Pd—N21 and Cl22—Pd—Cl23 angles are 80.529° and 95.090°, respectively. It was found that the N11—Pd—N21 is smaller than that found in cis-platin (NH_3—Pt—NH_3) by 6.471° and this can be interpreted in terms of CH_2 group, which connects the two coordination sites (N11 and N21) and prevent opening of this angle. The calculated Cl22—Pd—Cl23 angle is larger than the experimental one in cis-platin molecule by about 3.19° [57]. This indicates that in a bare palladium complex (in gas phase), the intramolecular hydrogen bonding N21—H27···Cl22 (2.730 Å) opens up Cl22—Pd—Cl23 angle. On the other hand, the optimized N11—Pt—N21 angle in case of cis-PtL^2Cl_2 is close to that found in cis-PdL^2Cl_2 complex, while the Cl22PtC23 angle is slight smaller than that exist in cis-platin by about 1.50°. This indicates that there is weak or no intramolecular hydrogen bonding as found in the PdL^2Cl_2 and this may be attributed to the significant difference in the bending angle of aniline ring as previously mentioned.

It was found that the C13N11 and C13N12 bond distances of the benzimidazole ring in the cis-PdL^2Cl_2 **(2)** and cis-PtL^2Cl_2 (**4**) complexes were increased upon the interaction of the pyridine-type nitrogen with the metal centre as compared with the L^2 ligand (Table 10). In addition, the C14N28 and C15N28 bond distances were enlarged upon the coordination of the secondary amino group to the metal centre. The benzimidazole nitrogen—Pd bond distance is 2.071 Å which coincide with that observed in the crystal structures of some benzimidazole complexes [58]. The Pd—N21 bond distance to the secondary nitrogen donor is 2.167 Å which is in a good agreement with the average value of 2.165 Å observed for *sec*-NH donor groups accompanied in some benzimidazole complexes e.g. nickel complex of N,N-bis(benzimid- azol-2-yl-

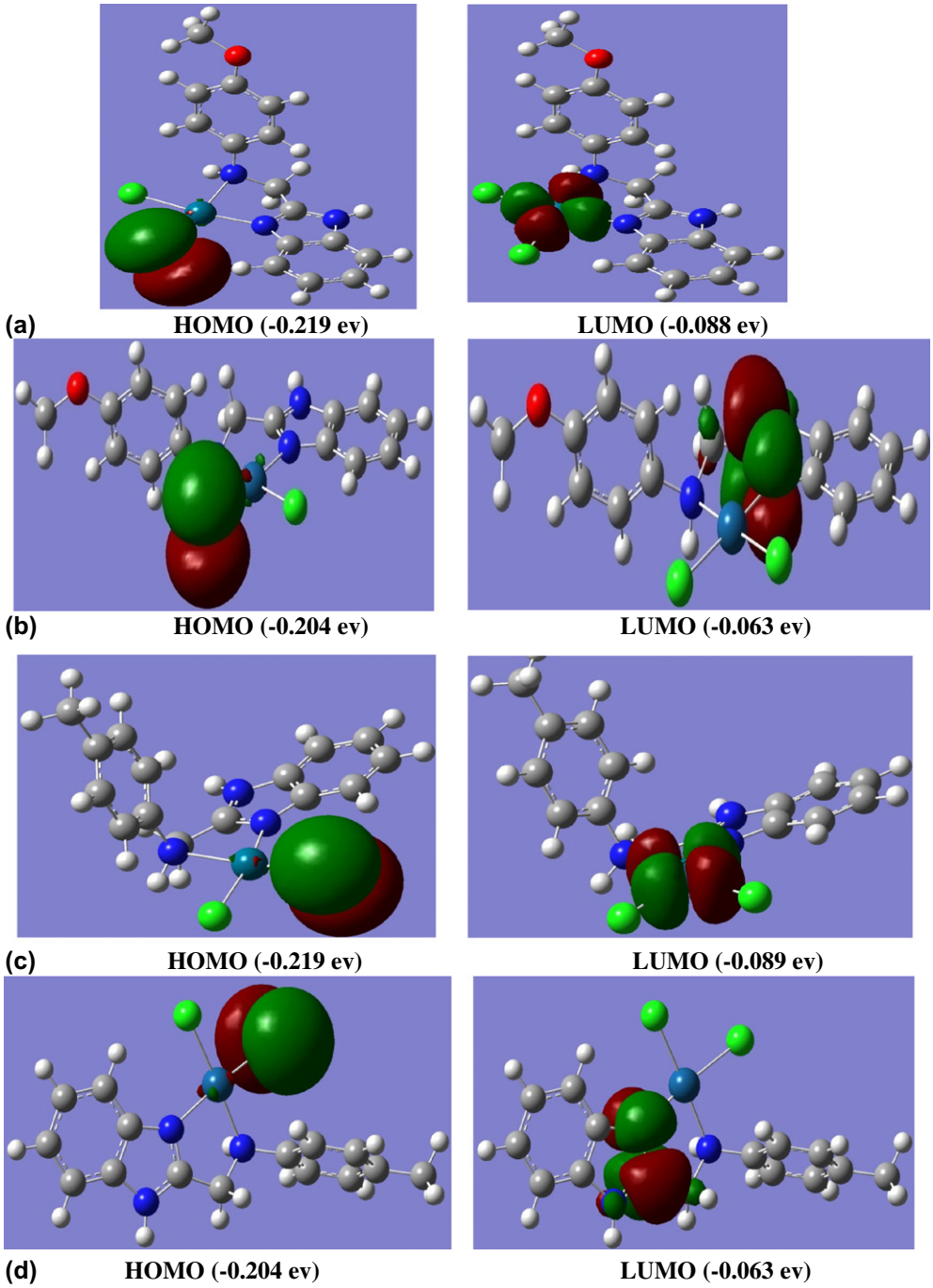

Fig. 7. Molecular orbital surfaces and energy levels of (a) Pd–L^1 (b) Pt–L^1 (c) Pd–L^2 (d) Pt–L^2.

methyl)amine [59]. The dipole moment increases spectacularly from a value of 3.969 D (L^2 derivative) to 14.979 D (Pd–L^2) and 15.347 (Pt–L^2), where the electropositive metal ions induce strong polarization in the σ- and π-frameworks of the ligand molecule. In addition, the energies of the Pd–L^2 and Pt–L^2 become more negative indicate the high stability of these complexes with respect to the free ligands.

The natural bond orbital (NBO) analysis of PtL^2Cl_2 complex for example was performed and could be used to estimate the delocalization of electron density between occupied Lewis-type orbitals and formally unoccupied non-Lewis NBOs (antibonding or Rydberg), which corresponds to a stabilizing donor–acceptor interaction [60]. Tables 9 and 10 collect the natural charges on atoms. The largest negative charges (−0.560e and −0.603e) are located on two nitrogen atoms, N11 and N21, respectively. According to the NBO, the electron configuration of Pt is: [core]$6s^{0.56}5d^{8.78}6p^{0.03}6d^{0.01}$. Thus, 68 core electrons, 9.34 valence electrons (on 6s and 5d atomic orbitals) and 0.04 Rydberg electrons (mainly on 6p and 6d orbitals) give the 77.380 electrons. This is consistent with the calculated natural charge on Pt atom (+0.620) in Pt–L^2 complex, which corresponds to the difference between 77.380e and the total number of electrons in the isolated Pt atom (78e). In addition, the two chlorine atoms (Cl22 and Cl23) coordinated to platinum atom have larger negative charge −0.552e and −0.508e, respectively. Thus, the positive atomic charge upon the Pt(II) was substantially reduced as a consequence of electron density donation from the pyridine-type nitrogen, secondary amino group and two chlorine atoms. The charges on N11 and N21 atoms

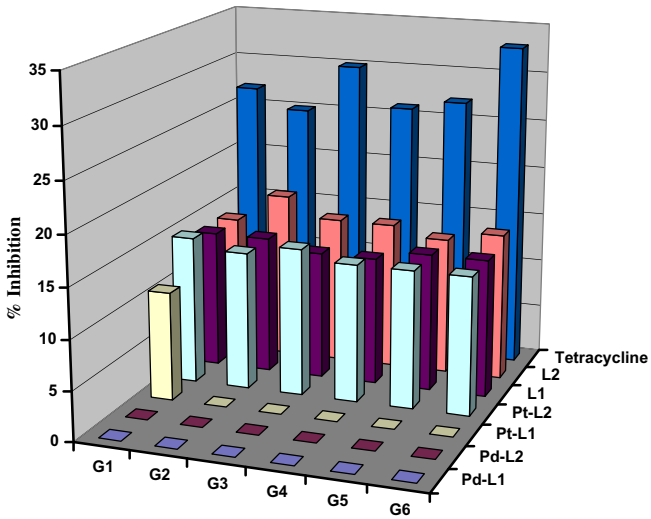

Fig. 8. Antibacterial activities of ligands $L^{1,2}$ and their complexes; Pd–$L^{1,2}$ and Pt–$L^{1,2}$ against *Bacillus subtilis* (G1), *Staphylococcus aureus* (G2), *Streptococcus faecalis* (G3) as Gram-positive, (G4) *Pseudomonas aeruginosa* (G4), *Escherichia coli* (G5), *Neisseria gonorrhoeae* (G6) as Gram-negative bacteria.

are not the same. It confirms that the electron density delocalized from the two nitrogen atoms to the metal ion is not the same, which is in agreement with the different bond lengths of PtN11 and PtN21. The atomic charges of the remaining atoms of the framework are reasonable according to electronegativity considerations. While in case of PdL^2Cl_2, the electron configuration of Pd is: $[core]5s^{0.35}4d^{8.93}5p^{0.02}5d^{0.01}6p^{0.01}$, with 36 core electrons, 9.28 valence electrons (on 5s and 4d atomic orbitals) and 0.037 Rydberg electrons (mainly on 5d and 6p orbitals) giving total 45.312 electrons. Similar, the charges on N11 and N21 atoms are not the same; with the different bond lengths of PdN11 and PdN21; as found in Pt–L^2 complex.

Table 11 lists the calculated occupancies of natural orbitals in Pt–L^2. Three classes of NBOs are included, the Lewis-type (s and p bonding or lone pair) orbitals, the valence non-Lewis (acceptors, formally unfilled) orbitals and the Rydberg NBOs, which originate from orbitals outside the atomic valence shell. The calculated natural hybrids on atoms are also given in Table 11. According to calculations, the platinum atom forms two sigma bonds with two chlorine atoms, while the two bonds between platinum and the nitrogen atoms can be described as donation of electron density from a lone pair (LP) orbital on each nitrogen atom to platinum molecular orbitals. As follows from Table 10, the σ(Pt—Cl22) bond

Table 7
Geometrical parameters optimized in L^1 derivative: bond length (Å), bond angles (°) and charges.

Bond lengths (Å)	B3LYP/6-31G(d)	B3LYP/LANL2DZ	Bond angles (°)	B3LYP/6-31G(d)	B3LYP/LANL2DZ	Charge B3LYP/6-31G(d)
C1C2	1.415	1.428	C2C1C6	122.584	122.379	C1 = 0.353
C2C3	1.399	1.404	C1C2C3	119.808	120.125	C2 = 0.238
C3C4	1.392	1.406	C2C3C4	118.006	117.893	C3 = −0.179
C4C5	1.409	1.421	C3C4C5	121.409	121.346	C4 = −0.143
C5C6	1.393	1.404	C4C5C6	121.524	121.516	C5 = −0.148
C1C6	1.395	1.407	C5C6C1	116.669	116.740	C6 = −0.174
C13C14	1.502	1.506	N11C13N12	112.976	112.271	C13 = 0.514
C15C16	1.404	1.417	C2N11C13	105.274	105.790	C14 = −0.173
C16C17	1.394	1.405	C1N12C13	107.164	107.440	C15 = 0.356
C17C18	1.400	1.410	C13C14N28	109.331	109.079	C16 = −0.203
C18C19	1.398	1.407	C14N28C15	120.610	123.538	C17 = −0.198
C19C20	1.392	1.402	C20C15N28	122.363	122.029	C18 = 0.369
C15C20	1.409	1.421	C15C16C17	121.523	121.339	C19 = −0.184
C13N11	1.310	1.330	C16C17C18	120.124	120.009	C20 = −0.183
C13N12	1.377	1.395	C17C18C19	118.896	119.331	H7 = 0.140
C14N28	1.445	1.448	C19C20C15	120.851	120.656	H8 = 0.128
C15N28	1.397	1.395	C16C15C20	117.739	120.790	H9 = 0.129
C18O30	1.373	1.407	C18O30C31	117.801	118.004	H10 = 0.128
C31O30	1.415	1.452	H22C14H23	106.053	106.151	H21 = 0.332
C3H7	1.086	1.086	C15N28H29	115.373	120.804	H22 = 0.161
C4H8	1.086	1.087	C14N28H29	111.599	115.656	H23 = 0.153
C5H9	1.086	1.087	C13N12H21	126.191	126.042	H24 = 0.123
C6H10	1.086	1.087	H7C3C4	121.712	121.684	H25 = 0.128
C14H22	1.107	1.107	H8C4C5	119.077	119.074	H26 = 0.132
C14H23	1.102	1.107	H9C5C6	119.167	119.306	H27 = 0.119
C16H24	1.088	1.089	H10C6C1	122.026	122.253	H32 = 0.146
C17H25	1.084	1.086	H24C16C17	119.213	119.369	H33 = 0.164
C19H26	1.086	1.086	H25C17C18	121.041	121.133	H34 = 0.147
C20H27	1.086	1.086	H26C19C20	120.591	118.536	N11 = −0.574
C31H32	1.099	1.100	H27C20C15	120.323	118.734	N12 = −0.745
C31H33	1.092	1.092				N28 = −0.676
C31H34	1.099	1.100				O30 = −0.515
N12H21	1.009	1.011				
N28H29	1.015	1.014				

	B3LYP/6-31G(d)	B3LYP/LANL2DZ
E (a.u.)	−820.104	−819.975
Zero-point *E* (kcal mol^{-1})	174.226	174.587
Rotational constants (GHz)	1.779, 0.116, 0.109	1.832, 0.112, 0.106
Entropy (cal mol^{-1} K^{-1})		
Translational	42.486	42.486
Rotational	33.924	33.953
Vibrational	54.552	54.544
Total dipole moment (D)	2.296	2.956

Table 8
Geometrical parameters optimized in L^2 derivative: bond length (Å), bond angles (°) and charges.

Bond lengths (Å)	B3LYP/6-31G(d)	B3LYP/LANL2DZ	Bond angles (°)	B3LYP/6-31G(d)	B3LYP/LANL2DZ	Charge B3LYP/6-31G(d)
C1C2	1.415	1.428	C2C1C6	122.579	120.132	C1 = 0.353
C2C3	1.399	1.403	C1C2C3	119.820	122.375	C2 = 0.238
C3C4	1.391	1.405	C2C3C4	117.996	116.735	C3 = −0.178
C4C5	1.408	1.420	C3C4C5	121.409	121.522	C4 = −0.143
C5C6	1.393	1.404	C4C5C6	121.528	121.342	C5 = −0.148
C1C6	1.395	1.406	C5C6C1	116.664	117.891	C6 = −0.174
C13C14	1.501	1.505	N11C13N12	112.987	112.270	C13 = 0.514
C15C16	1.409	1.421	C2N11C13	105.276	105.795	C14 = −0.170
C16C17	1.387	1.399	C1N12C13	107.149	107.437	C15 = 0.359
C17C18	1.404	1.416	C13C14N28	109.306	109.077	C16 = −0.188
C18C19	1.396	1.408	C14N28C15	121.275	123.553	C17 = −0.184
C19C20	1.397	1.408	C20C15N28	122.544	122.279	C18 = 0.178
C15C20	1.404	1.417	C15C16C17	120.806	120.716	C19 = −0.196
C13N11	1.309	1.329	C16C17C18	121.735	121.759	C20 = −0.180
C13N12	1.376	1.394	C17C18C19	117.116	117.204	H7 = 0.140
C14N28	1.443	1.448	C19C20C15	120.421	121.942	H8 = 0.128
C15N28	1.390	1.391	C16C15C20	117.897	120.427	H9 = 0.128
C3H7	1.085	1.085	H22C14H23	106.050	106.170	H10 = 0.128
C4H8	1.086	1.087	C15N28H33	116.223	120.798	H21 = 0.331
C5H9	1.086	1.087	C14N28H33	112.264	115.646	H22 = 0.162
C6H10	1.086	1.086	C13N12N21	126.222	126.041	H23 = 0.154
C14H22	1.106	1.106	H7C3C4	121.716	121.683	H24 = 0.121
C14H23	1.101	1.106	H8C4C5	119.078	119.075	H25 = 0.117
C16H24	1.088	1.088	H9C5C6	119.162	119.300	H26 = 0.114
C17H25	1.088	1.089	H10C6C1	122.030	122.246	H27 = 0.114
C19H26	1.088	1.089	H24C16C17	120.000	120.038	H30 = 0.154
C20H27	1.085	1.086	H25C17C18	119.412	119.322	H31 = 0.149
C29H30	1.097	1.099	H26C19C20	118.671	118.761	H32 = 0.156
C29H31	1.095	1.096	H27C20C15	120.395	120.501	H33 = 0.348
C29H32	1.098	1.099				N11 = −0.574
N12H21	1.009	1.010				N12 = −0.745
N28H33	1.014	1.014				N28 = −0.677
C18C29	1.511	1.519				C29 = −0.677

	B3LYP/6-31G(d)	B3LYP/LANL2DZ
E (a.u.)	−744.902	−744.781
Zero-point *E* (kcal mol^{-1})	170.955	171.763
Rotational constants (GHz)	1.934, 0.140, 0.131	1.962, 0.137, 0.128
Entropy (cal mol^{-1} K^{-1})		
Translational	42.292	42.292
Rotational	33.470	33.505
Vibrational	52.801	51.401
Total dipole moment (D)	3.386	3.969

is formed from an $sp^{0.01}d^{1.19}$ hybrid on platinum atom (which is the mixture of 45.58s, 0.30p and 54.12%d atomic orbitals) and $sp^{8.89}$ hybrid on the chlorine atom (89.89%p contribution). The results from NBO analysis show that the σ(Pt—Cl22) bond is strongly polarized towards the chloride, with about 75.28% of electron density concentrated on the chlorine atom, i.e. about 75.28% of electron density is accommodated on the Cl atom. The strength of this interaction can be estimated by the second order perturbation theory.

Table 12 lists the selected values of the calculated second order interaction energy (E^2) between donor–acceptor orbitals in Pt–L^2 complex. The strongest interactions are the electron donations from a lone pair orbital on the nitrogen atoms, LP(1)N11 to the antibonding acceptor σ*(Pt—Cl22) orbitals, i.e. LP(1)N11 → σ*(Pt—Cl22). As shown in Table 10, the LP(1)N11 orbital has 70.59% p-character and is occupied by 1.698 electrons (this is consistent with a delocalization of electron density from the idealized occupancy of 2.0e). The donation of electron density from the coordination sites in the ligand to the Pt molecular orbitals has a clear correspondence to a chemical picture of the coordination bonds.

The frontier molecular orbitals play also an important role in the electric and optical properties, as well as in UV/vis. spectra and chemical reactions [61]. Fig. 7 show the distributions and energy levels of the HOMO, and LUMO orbitals computed at the B3LYP/LANL2DZ level for Pd–$L^{1,2}$ and Pt–$L^{1,2}$ complexes. The value of the energy separation between the HOMO and LUMO is 0.131, 0.141, 0.130, and 0.141 eV for cis-PdL^1Cl_2, cis-PtL^1Cl_2, cis-PdL^2Cl_2, and cis-PtL^2Cl_2, respectively.

3.9. Biological activity

3.9.1. Antimicrobial activity

The data showed that the ligands $L^{1,2}$ have the capacity of inhibiting the metabolic growth of the investigated bacteria; *B. subtilis*, *S. aureus* and *S. faecalis* as Gram-positive bacteria and *P. aeruginosa*, *E. coli* and *N. gonorrhoeae* as Gram-negative bacteria; to different extents as shown in Fig. 8. The size of the inhibition zone depends upon the culture medium, incubation conditions, rate of diffusion and the concentration of the antibacterial agent (the activity increases as the concentration increases). In classifying the antibacterial activity as Gram-positive or Gram-negative, it would generally be expected that a much greater number of drugs would be active against Gram-positive than Gram-negative bacteria. However, in this study, $L^{1,2}$ are active against both types of the bacteria, which may indicate broad-spectrum properties. The remarkable activity of these compounds may be arising from the benzimidazole ring, which may play an important role in the antibacterial activity. The mode of action may involve the formation of a hydrogen bond through the tertiary nitrogen of the imidazole

Table 9
Selected bond lengths (Å), angles (°) and charge for Pd–L[1] and Pt–L[1].

Pd–L[1]					Pt–L[1]				
Bond lengths (Å)		Bond angles (°)		Charge	Bond lengths (Å)		Bond angles (°)		Charge
C1C2	1.425	C1C2C3	121.017	C1 = 0.151	C1C2	1.425	C1C2C3	120.728	C1 = 0.153
C2C3	1.406	C2C3C4	116.987	C2 = 0.149	C2C3	1.406	C2C3C4	117.091	C2 = 0.149
C3C4	1.402	C3C4C5	121.736	C3 = −0.187	C3C4	1.403	C3C4C5	121.847	C3 = −0.186
C4C5	1.422	C4C5C6	121.652	C4 = −0.214	C4C5	1.421	C4C5C6	121.483	C4 = −0.214
C5C6	1.404	C5C6C1	116.492	C5 = −0.199	C5C6	1.404	C5C6C1	116.527	C5 = −0.198
C2N11	1.409	C6C1C2	122.116	C6 = −0.250	C2N11	1.415	C6C1C2	122.323	C6 = −0.252
C1N12	1.410	C2N11C13	107.554	N11 = −0.560	C1N12	1.408	C2N11C13	107.330	N11 = −0.561
C13N11	1.337	C1N12C13	107.666	N12 = −0.603	C13N11	1.338	C1N12C13	107.701	N12 = −0.599
C13N12	1.378	N11C13N12	111.183	C13 = 0.473	C13N12	1.377	N11C13N12	111.378	C13 = 0.473
C13C14	1.505	C13C14N21	108.252	C14 = −0.252	C13C14	1.496	C13C14N21	109.059	C14 = −0.243
C14N21	1.502	C14N21C15	116.648	C15 = 0.139	C14N21	1.521	C14N21C15	111.061	C15 = 0.142
C15N21	1.468	N21C15C16	118.460	C16 = −0.203	C15N21	1.478	N21C15C16	119.807	C16 = −0.214
C15C16	1.406	C15C16C17	120.408	C17 = −0.281	C15C16	1.409	C15C16C17	119.716	C17 = −0.219
C16C17	1.404	C16C17C18	119.858	C18 = 0.331	C16C17	1.396	C16C17C18	120.161	C18 = 0.338
C17C18	1.411	C17C18C19	119.717	C19 = −0.226	C17C18	1.414	C17C18C19	120.111	C19 = −0.289
C18C19	1.410	C18C19C20	120.253	C20 = −0.247	C18C19	1.409	C18C19C20	119.311	C20 = −0.217
C19C20	1.401	C19C20C15	120.105	N21 = −0.688	C19C20	1.409	C19C20C15	120.323	N21 = −0.695
C15C20	1.411	C20C15C16	119.653	Cl22 = −0.555	C15C20	1.399	C20C15C16	120.365	Cl22 = −0.518
C18O33	1.393	N11PdN21	80.569	Cl23 = −0.511	C18O33	1.392	C18O33C34	118.786	Cl23 = −0.498
N11Pd	2.071	Cl22PdCl23	95.215	Pd = 0.687	O33C34	1.458	N11PtN21	81.287	Pt = 0.619
N21Pd	2.163			O33 = −0.566	N11Pt	2.054	Cl22PtCl23	90.444	O33 = −0.563
Cl22Pd	2.391			C34 = −0.262	N21Pt	2.150			C34 = −0.263
Cl23Pd	2.371				Cl22Pt	2.400			
					Cl23Pt	2.398			
E (a.u.)				−976.728		−969.141			
Zero-point *E* (kcal mol^{-1})				178.647		178.603			
Rotational constants (GHz)				0.261, 0.140, 0.107		0.405, 0.107, 0.089			
Entropy (cal mol^{-1} K^{-1})									
Translational				44.059		44.621			
Rotational				35.660		35.676			
Vibrational				74.764		75.732			
Total dipole moment (D)				13.865		15.714			

Table 10
Selected bond lengths (Å), angles (°) and charge for Pd–L[2] and Pt–L[2].

Pd–L[2]					Pt–L[2]				
Bond lengths (Å)		Bond angles (°)		Charge	Bond lengths (Å)		Bond angles (°)		Charge
C1C2	1.425	C1C2C3	121.037	C1 = 0.151	C1C2	1.424	C1C2C3	120.721	C1 = 0.153
C2C3	1.406	C2C3C4	116.983	C2 = 0.149	C2C3	1.407	C2C3C4	117.09	C2 = 0.149
C3C4	1.402	C3C4C5	121.728	C3 = −0.187	C3C4	1.402	C3C4C5	121.844	C3 = −0.186
C4C5	1.422	C4C5C6	121.661	C4 = −0.214	C4C5	1.421	C4C5C6	121.489	C4 = −0.214
C5C6	1.404	C5C6C1	116.492	C5 = −0.199	C5C6	1.403	C5C6C1	116.526	C5 = −0.198
C2N11	1.409	C6C1C2	122.098	C6 = −0.251	C2N11	1.415	C6C1C2	122.326	C6 = −0.252
C1N12	1.410	C2N11C13	107.572	N11 = −0.560	C1N12	1.409	C2N11C13	107.335	N11 = −0.561
C13N11	1.336	C1N12C13	107.668	N12 = −0.603	C13N11	1.338	C1N12C13	107.694	N12 = −0.599
C13N12	1.378	N11C13N12	111.171	C13 = 0.474	C13N12	1.377	N11C13N12	111.343	C13 = 0.473
C13C14	1.505	C13C14N21	108.290	C14 = −0.252	C13C14	1.496	C13C14N21	108.843	C14 = −0.244
C14N21	1.502	C14N21C15	116.773	C15 = 0.155	C14N21	1.522	C14N21C15	110.589	C15 = 0.156
C15N21	1.467	N21C15C16	118.255	C16 = −0.215	C15N21	1.480	N21C15C16	119.575	C16 = −0.232
C15C16	1.410	C15C16C17	119.728	C17 = −0.196	C15C16	1.402	C15C16C17	119.626	C17 = −0.207
C16C17	1.401	C16C17C18	121.548	C18 = −0.004	C16C17	1.409	C16C17C18	120.962	C18 = 0.004
C17C18	1.415	C17C18C19	117.764	C19 = −0.204	C17C18	1.410	C17C18C19	118.172	C19 = −0.196
C18C19	1.409	C18C19C20	121.445	C20 = −0.253	C18C19	1.415	C18C19C20	121.384	C20 = −0.214
C19C20	1.408	C19C20C15	119.749	N21 = −0.690	C19C20	1.401	C19C20C15	119.327	N21 = −0.696
C15C20	1.406	C20C15C16	119.764	Cl22 = −0.552	C15C20	1.405	C20C15C16	120.522	Cl22 = −0.516
C18C32	1.517	N11PdN21	80.529	Cl23 = −0.508	C18C33	1.517	N11PtN21	81.128	Cl23 = −0.497
N11Pd	2.071	Cl22PdCl23	95.090	Pd = 0.688	N11Pt	2.054	Cl22PtCl23	90.398	Pt = 0.61962
N21Pd	2.167			C32 = −0.650	N21Pt	2.150			C33 = −0.651
Cl22Pd	2.389				Cl22Pt	2.399			
Cl23Pd	2.370				Cl23Pt	2.398			
E (a.u.)				−901.532		−893.946			
Zero-point *E* (kcal mol^{-1})				175.724		175.699			
Rotational constants (GHz)				0.276, 0.171, 0.125		0.413, 0.130, 0.104			
Entropy (cal mol^{-1} K^{-1})									
Translational				43.945		44.528			
Rotational				35.255		35.303			
Vibrational				71.919		72.644			
Total dipole moment (D)				14.979		15.347			

Table 11
Occupancy of natural orbitals (NBOs) and hybrids calculated for Pt–L^2 (selected).

Donor[a] Lewis-type NBOs (A-B)	Occupancy	Hybrid[b]	AO (%)[c]	Acceptor[d] non–Lewis NBOs	NBOs
σ(C2—N11)	1.978	$sp^{1.86}$ (N11) $sp^{2.59}$ (C2)	s(34.96)p(65.04) s(27.85)p(72.15)	σ*(C2—N11)	0.036
σ(C13—N11)	1.978	$sp^{1.80}$ (N11) $sp^{2.14}$ (C13)	s(35.65)p(64.35) s(31.88)p(68.12)	σ*(C13—N11)	0.026
π(C13—N11)	1.899	sp (N11) sp (C13)	p(100.00) s(0.01)p(99.99)	π*(C13—N11)	0.441
σ(C14—N21)	1.975	$sp^{2.94}$ (N21) $sp^{3.52}$(C14)	s(25.40)p(74.60) s(22.15)p(77.85)	σ*(Cl4—N21)	0.028
σ(C15—N21)	1.983	$sp^{2.01}$ (N21) $sp^{2.91}$ (C15)	s(33.22)p(66.78) s(25.56)p(74.44)	σ*(C15—N21)	0.041
σ(Pt—Cl22)	1.966	$sp^{0.01}d^{1.19}$ (Pt) $sp^{8.89}$(C122)	s(45.58)p(0.30)d(54.12) s(10.11)p(89.89)	σ*(Pt—Cl22)	0.313
σ(Pt—Cl23)	1.968	$sp^{0.01}d^{1.12}$ (Pt) $sp^{9.12}$ (C123)	s(46.97)p(0.36)d(52.86) s(9.79)p(90.12)	σ*(Pt—Cl23)	0.286
σ(N21—H27)	1.981	$sp^{3.07}$ (N21)	s(24.57)p(75.43)		
LP(1)N11	1.698	$sp^{2.40}$	s(29.41)p(70.59)	RY*(1)N11	0.004
LP(1)N21	1.718	$sp^{4.95}$	s(16.80)p(83.20)	RY*(1)N21	0.009
LP(1)Cl22	1.993	$sp^{0.26}$	s(79.40)p(20.60)	RY*(1)Cl22	0.0003
LP(1)Cl23	1.993	$sp^{0.26}$	s(79.65)p(20.35)	RY*(1)Cl23	0.0004
LP(1)Pt	1.993	$sp^{0.06}d^{49.45}$	s(1.98)p(0.13)d(97.89)	RY*(1)Pt	0.020
LP(2)Pt	1.986	$sp^{0.01}d^{19.99}$	s(4.76)p(0.06)d(95.18)	RY*(2)Pt	0.004
LP(3)Pt	1.980	$sp^{1.00}d^{99.99}$	s(0.01)p(0.06)d(99.94)	RY*(3)Pt	0.002

[a] LP(*n*)A is a valence lone pair orbital (n) on A atom.
[b] Hybrid on A atom in the A—B bond or otherwise, as indicated.
[c] Percentage contribution of atomic orbitals in NBO hybrid.
[d] Starred label (*) denotes antibonding, and Ry corresponds to the Rydberg NBO orbital.

ring with the active centers of the cell constituents, resulting in interference with the normal cell process [62].

It is known that the chelation process facilitates the ability of a complex to cross a cell membrane and can be explained by Tweedy's chelation theory [63]. However, the Pt–L^2 complex shows activity comparable to that found in the uncoordinated ligand (L^2) suggesting that the platinum atom has no responsibility in the activity of this compound. In addition, the Pt–L^1 complex was inactive against all the tested bacteria except the Gram-positive bacterium *Bacillus subtilis* with activity lower than found in the uncoordinated ligand. Comparison between the two platinum complexes confirms the role of the methyl group in the inhibition process. On the other hand, the Pd–$L^{1,2}$ complexes are inactive against all the tested organisms and the possible explanation for these results is their inability to chelate metals essential for the metabolism of microorganisms and/or to form hydrogen bonds with the active centers of cell structures, resulting in an interference with the normal cell cycle. Furthermore, the low activity of these complexes may be also due to their low lipophilicity, because of which penetration of the complex through the lipid membrane was decreased and hence, they could neither block nor inhibit the growth of the microorganism.

Therefore, we confirm that the toxicity of the complexes can be related to the strengths of the metal–ligand bond, besides other factors such as size of the cation, receptor sites, diffusion and a combined effect of the metal and the ligands for inactivation of the biomolecules, as previously reported by other authors [64].

Table 12
Second-order interaction energy (E^2, kcal/mol) between donor and acceptor orbitals in Pt–L^2 complex calculated at B3LYP/LANL2DZ level of theory (selected).

Donor → Acceptor	E^2	Donor → Acceptor	E^2
LP(1)N11 → σ*(Pt—Cl22)	98.31	σ(N11—C13) → σ*(Pt—Cl22)	6.08
LP(1)N21 → σ*(Pt—Cl23)	76.30	σ(N21—H27) → σ*(Pt—Cl23)	5.95
σ(Pt—Cl23) → σ*(Pt—Cl22)	4.70	σ(N21—C14) → σ*(Pt—Cl23)	2.89

3.9.2. Antitumor activity

To evaluate the potential usefulness of Pd–$L^{1,2}$ and Pt–$L^{1,2}$ complexes synthesized as antitumor agents, three cell lines of different origin; *breast cancer* (MCF-7), *Colon carcinoma* (HCT) and *human heptacellular carcinoma* (Hep-G2) were treated at the concentration of 100 μM. All the compounds showed activity against all the studied cell lines. On screening against HCT cells, it was found that all the complexes show similar activity; irrespective of changing the types of metals and ligands; but lower than found in cis-platin. The remarkable activity of these complexes may be arising from the benzimidazole ring itself. In case of MCF-7 cells, the Pd–L^1 and Pt–$L^{1,2}$ complexes are more toxic than cis-platin with the order Pt–L^1 > Pd–L^1 > Pt–L^2 suggesting that the methoxyl group plays a role in the cytotoxicity of these complexes through the important hydrogen-bond donor properties, either in the approach of the biological target or the final structure. For Hep-G2 cells, it was found that all the complexes show higher activity than cis-platin with the order Pt–L^1 > Pd–L^2 > Pd–L^1 > Pt–L^2. The high toxicity of Pd–$L^{1,2}$ complex than Pt–L^2 happens because the ligand-exchange behavior of platinum compound is quite slow, which gives them a high kinetic stability and results in ligand-exchange reactions within minutes to days, rather than microseconds to seconds for many other coordination compounds. In addition, another unusual phenomenon deals with the preferred ligands for platinum ions is that Pt(II) has a strong thermodynamic preference for binding to S-donor ligands and for this reason, one would predict that platinum compounds would perhaps never reach DNA, with many cellular platinophiles (S-donor ligands, such as glutathione, methionine) as competing ligands in the cytosol [65]. In addition, Pt–L^1 complex shows the same cyctotoxic activity against the MCF-7 and Hep-G2 cell lines and twice that found against HCT cells.

4. Conclusion

Owing to the antibacterial activity of the benzimidazole ring, it was found that the studied benzimidazole ligands have the capacity

of inhibiting the metabolic growth of the investigated bacteria to different extent and these benzimidazoles $L^{1,2}$ are more toxic than their metal complexes. This may be attributed to the inability of the complexes to chelate metals essential for the metabolism of microorganisms and/or to form hydrogen bonds with the active centers of cell structures, resulting in an interference with the normal cell cycle. All the studied complexes showed activity against three cell lines of different origin, *breast cancer* (MCF-7), *Colon carcinoma* (HCT) and *human heptacellular carcinoma* (Hep-G2) and represent an interesting class of new compounds from the viewpoint of their physicochemical and structural properties. The results obtained can be useful in having of an understanding of the factors that influence activity of the complexes and in supporting the general assumption that relationship between structure and activity is extremely complex. On the basis of the agreement between the calculated and experimental results, assignments of all the fundamental vibrational modes of benzimidazole L were examined and proposed at higher level of theory. The natural bond orbital (NBO) analysis has provided the detailed insight into the type of hybridization and the nature of bonding in the studied complexes. Comparison has been done with the data obtained for cis-platin. The strong coordination bonds (LP(1)N11 → σ^*(Pd—Cl22)) and (LP(1)N21 → σ^*(Pd—Cl23)) result from donation of electron density from a lone pair orbital on the nitrogen atoms to the acceptor palladium molecular orbitals. Based on the results obtained from the physico-chemical techniques and theoretical calculation of the metal complexes; one can conclude that the studied ligands behave as neutral bidentate ligands coordinated to the metal ions via he pyridine-type nitrogen of the benzimidazole ring and secondary amino group. Thus, square-planar geometry is suggested for all the studied complexes; $[PdL^1Cl_2]\cdot 3H_2O$, $[PtL^1Cl_2]\cdot H_2O$, $[PdL^2Cl_2]$ and $[PtL^2Cl_2]\cdot 2H_2O$.

Acknowledgments

We would like to extend our grateful thanks to Prof. Rifaat Hilal, Chemistry Department, Faculty of Science, Cairo University for allowing us to use his version of the *Guassian98W* package of programs. Deep thanks to Prof. Dr. Samia Showman, professor of Medical Biochemistry, National Cancer Centre, Cairo University, for the great helps and support during the biological part.

References

[1] (a) I.H. Krakoff, in: M. Nicali (Ed.), Platinum and Other Metal Coordination Compounds in Cancer Chemotherapy, Clinical Application of Platinum Complexes, Martinus Nijhoff, Boston, MA, 1988, p. 351;
(b) E.R. Jamieson, S.J. Lippard, Chem. Rev. 99 (1999) 2467–2498.
[2] I. Kostova, Recent Patents on Anti-Cancer Drug Discovery 1 (2006) 1–22.
[3] (a) F. Gumus, G. Eren, L. Acik, A. Celebi, F. Ozturk, R. Ilikci Sagkan, S. Gur, A. Ozkul, A. Elmali, Y. Elerman, J. Med. Chem. 52 (5) (2009) 1345–1357;
(b) M. Goekce, S. Utku, S. Guer, A. Oezkul, F. Gumus, Eur. J. Med. Chem. 40 (2) (2005) 135–141;
(c) F. Gumus, O. Algul, G. Eren, H. Eroglu, N. Diril, S. Gur, A. Ozkul, Eur. J. Med. Chem. 38 (5) (2003) 473–480;
(d) F. Gumus, A.B. Demirci, T. Oezden, H. Eroglu, N. Diril, Pharmazie 58 (5) (2003) 303–307;
(e) F. Gumus, I. Pamuk, T. Oezden, S. Yildiz, N. Diril, E. Oksuzoglu, S. Gur, A. Ozkul, J. Inorg. Biochem. 94 (3) (2003) 255–262.
[4] (a) V. Rajendiran, M. Murali, E. Suresh, S. Sinha, K. Somasundaram, M. Palaniandavar, Dalton Trans. (2008) 148;
(b) J. Mann, A. Baron, Y. Opoku-Boahen, E. Johansson, G. Parkinson, L.R. Kelland, S. Neidle, J. Med. Chem. 44 (2001) 138.
[5] J.B. Camden, US Patent 6,077,862, 2002.
[6] P.K. Naithani, V.K. Srivastava, A.K. Saxena, J.P. Barthwal, T.K. Gupta, K. Shanker, Indian J. Exp. Biol. 28 (1990) 1145.
[7] N.M. Goudgaon, V. Dhondiba, A. Vijayalaxmi, Indian J. Heterocycl. Chem. 13 (2004) 271.
[8] (a) E. Bouwmann, W.L. Driessen, J. Reedijk, Coord. Chem. Rev. 104 (1990) 143;
(b) M.A. Puja, T.D. Bharamgouda, N.D. Sathyanarayna, Trans. Met. Chem. 13 (1988) 423.
[9] (a) Phillips, J. Chem. Soc. (1928) 2393;
(b) H. Skolnik, J. Miller, A.R. Day, J. Am. Chem. Soc. 65 (1943) 1854.
[10] A.D. Becke, J. Chem. Phys. 98 (1993) 5648.
[11] C. Lee, W. Yang, R.G. Parr, Phys. Rev. B. 37 (1998) 785.
[12] M.J. Frisch, G.W. Trucks, H.B. Schlegel, G.E. Scuseria, M.A. Robb, J.R. Cheeseman, V.G. Zakrzewski, J.A. Montgomery, R.E. Stratmann, J.C. Burant, S. Dapprich, J.M. Millam, A.D. Daniels, K.N. Kudin, M.C. Strain, O. Farkas, J. Tomasi, V. Barone, M. Cossi, R. Cammi, B. Mennucci, C. Pomelli, C. Adamo, S. Clifford, J. Ochterski, G.A. Petersson, P.Y. Ayala, Q. Cui, K. Morokuma, D.K. Malick, A.D. Rabuck, K. Raghavachari, J.B. Foresman, J. Cioslowski, J.V. Ortiz, A.G. Baboul, B.B. Stefanov, G. Liu, A. Liashenko, P. Piskorz, I. Komaromi, R. Gomperts, R.L. Martin, D.J. Fox, T. Keith, M.A. Al-Laham, C.Y. Peng, A. Nanayakkara, C. Gonzalez, M. Challacombe, P.M.W. Gill, B.G. Johnson, W. Chen, M.W. Wong, J.L. Andres, M. Head-Gordon, E.S. Replogle, J.A. Pople, GAUSSIAN 03 (Revision A.9), Gaussian, Inc., Pittsburgh, 2003.
[13] H.B. Schlegel, J. Comput. Chem. 3 (1982) 214.
[14] A. Frisch, A.B. Nielson, A.J. Holder, GAUSSVIEW User Manual, Gaussian Inc., Pittsburgh, PA, 2000.
[15] R. Ditchfield, Chem. Phys. 76 (1972) 5688.
[16] (a) D. Greenwood, Antimicrobial Chemotherapy, Bailliere, Tindall, London. Part II. Laboratory Aspects of Antimicrobial Therapy, 1983, p. 71.;
(b) V. Lorian, Antibiotics in Laboratory Medicine, Williams & Wilkins, Baltimore, 1996.
[17] National Committee for Clinical Laboratory Standards, NCCLS Approval Standard Document M2-A7, Vilanova, PA, 2000.
[18] C.M. Lozano, O. Cox, M.M. Muir, J.D. Morales, J.L. Rodríguez-Cabáin, P.E. Vivas-Mejfa, F.A. Gonzalez, Inorg. Chim. Acta 271 (1998) 137–144.
[19] (a) P. Skehan, R. Smreng, D. Scudiero, A. Monks, J. McMahon, D. Vistica, J.T. Warren, H. Bokesch, S. Kenney, M.R. Boyd, J. Nat. Cancer Inst. 82 (1990) 107–1112;
(b) A. Monks, D. Scudiero, P. Skehan, K. Paull, D. Vistica, C. Hose, J. Langley, P. Cronise, A. Viagro-Wolff, M. Gra-Goodrich, J. Nat. Cancer Inst. 83 (1991) 757–766.
[20] (a) G. Rauhut, P. Pulay, J. Phys. Chem. 99 (1995) 3093–3100;
(b) J.A. Pople, H. B. Schlegel, R. Krishnan, J.S. Defrees, J.S. Binkley, M.J. Frisch, R.A. Whiteside, Int. J. Quantum Chem.: Quantum Chem. Symp. 15 (1981) 269.
[21] (a) M.W. Ellzy, J.O. Jensen, H.F. Hameka, J.G. Kay, D. Zeroka, Spectrochim. Acta A 57 (2001) 2417;
(b) J.O. Jensen, A. Banerjee, C.N. Merrow, D. Zeroka, J.M. Lochner, J. Mol. Struct.: Theochem. 531 (2000) 323;
(c) J.O. Jensen, D. Zeroka, J. Mol. Struct.: Theochem. 487 (1999) 267.
[22] O. Sala, N.S. Goncalves, L.K. Noda, J. Mol. Struct. 411 (2001) 565–566.
[23] K. Hofmann, Imidazole and its Derivatives, Interscience Publishers, New York, 1953.
[24] S. Satyanarayana, K.R. Nagasundara, Synth. React. Inorg. Met.-org. Chem. 34 (5) (2004) 883–895.
[25] R.W. Hay, T. Clifford, P.L. Foot, Polyhedron 17 (20) (1998) 3575.
[26] S. Mohan, N. Sundaraganesan, Spectrochim. Acta A 47 (1991) 1111.
[27] N. Sundaraganesan, S. Ilakiamani, P. Subramani, B. Dominic Joshua, Spectrochim. Acta A 67 (2007) 628–635.
[28] N.M. Agathabay, M. Tulu, M. Somer, D. Haciu, A. Yilmaz, Struct. Chem. 19 (2008) 21.
[29] F.S. Miranda, F.G. Menezes, J. Vicente, A.J. Bortoluzzi, C. Zucco, A. Neves, N.S. Gonçalves, J. Mol. Struct. 938 (2009) 1–9.
[30] K. Nakamoto, "Infrared and Raman Spectra of Inorganic and Coordination Compounds", Part B: Applications in Coordination, Organometallic, and Bioinorganic Chemistry, sixth ed., John Wiley & Sons Inc., New Jersey, 2009.
[31] (a) V. Arjunan, I. Saravanan, P. Ravindran, S. Mohan, Spectrochim. Acta A 74 (2009) 642–649;
(b) P.S. Kalsi, Spectroscopy of Organic Compounds, sixth ed., New Age International (P) Limited Publishers, New Deihi, 2005.
[32] D.K. Lavallee, M.D. Baughman, M.P. Phillips, J. Am. Chem. Soc. 99 (1977) 718.
[33] W. Nawrocka, B. Sztuba, M.W. Kowalaka, H. Liszkiewicz, Farmaco 59 (2004) 83.
[34] N.M. Aghatabay, M. Somer, M. Senel, B. Dulger, F. Gucin, Eur. J. Med. Chem. 42 (2007) 1069–1075.
[35] M.R. Figueroa, D.E. Gomez, C.P. Iglesias, A. De Blas, T.R. Blas, Eur. J. Inorg. Chem. (2007) 2198.
[36] J.D. Crane, R. Hughes, E. Sinn, Inorg. Chim. Acta 237 (1995) 181–185.
[37] B. Blicharskaa, T. Kupka, J. Mol. Struct. 613 (2002) 153–166.
[38] R.M. Issa, A.A. Hassanein, I.M. El-Mehasseb, R.I.Abed. El-Wadoud, Spectrochim. Acta A 65 (2006) 206–214.
[39] M. Krishnamurthy, P. Phaniraj, S.K. Dogra, J. Chem. Soc. Perkin Trans. II (1986) 1917–1925. and the references therein.
[40] A.K. Mishra, S.K. Dogra, Bull. Chem. Soc. Jpn. 58 (1985) 3587;
A.K. Mishra, S.K. Dogra, J. Photochem. 31 (1985) 333;
A.K. Mishra, S.K. Dogra, Indian J. Phys., Sect. B 54 (1984) 480;
A.K. Mishra, S.K. Dogra, Spectrochim. Acta A 39 (1983) 609.
[41] G.G. Araya-Hernandez, R.G.E. morales, J. Photochem. Photobiol. A: Chem. 177 (2006) 125.
[42] R.M. Issa, S.A. El-Daly, N.A. El-Wakiel, Spectrochim. Acta A 59 (2003) 723–728.
[43] O.E. Offiong, S. Martelli, Trans. Met. Chem. 22 (1997) 263–269.
[44] (a) A.B.P. Lever, Inorganic Electronic Spectroscopy, second ed., Elsevier, Amsterdam, 1982. pp. 544–552;
(b) D.X. West, M.S. Lockwood, A. Liberta, X. Chen, R.D. Willet, Trans. Met. Chem. 18 (1993) 221.

[45] (a) I. Lakomska, M. Barwiolek, E. Szlyk, Trans. Met. Chem. 32 (2007) 70;
(b) A. Bakalova, H. Varbanov, R. Buyukliev, G. Momekov, D. Ivanov, J. Therm. Anal. Calorim. 95 (2009) 241–246.
[46] E.M. Abd Alla, M.I. Abdel-Hamid, J. Therm. Anal. Calorim. 76 (2000) 769–780.
[47] G. Faraglia, F. Barbaro, S. Sitran, Trans. Met. Chem. 15 (1990) 242–245.
[48] G. Singh, S.P. Felix, D.K. Pandey, Thermochim. Acta 411 (2004) 61–71.
[49] G. Singh, D.K. Pandey, Combust. Flame 135 (2003) 135–143.
[50] A.W. Coats, J.P. Redfern, Nature 201 (1964) 68.
[51] H.H. Horowitz, G. Metzger, Anal. Chem. 85 (1963) 1464.
[52] T. Hatakeyama, F.X. Quinn, Thermal Analysis, Fundamental and Applications to Polymer Science, John Wiley & Sons Ltd., 1999.
[53] B.D. Cullity, Elements of X-ray Diffraction, second ed., Addison-Wesley Inc., 1993.
[54] N. Vijayan, R. Ramesh Babu, R. Gopalakrishnan, P. Ramasamy, W.T.A. Harrison, J. Cryst. Growth 262 (2004) 490–498.
[55] R.I. Castillo, S.P.H. Rivera, J. Mol. Struct. 917 (2009) 158–163.
[56] D.N. Neogi, P. Das, A.N. Biswas, P. Bandyopadhyay, Polyhedron 25 (2006) 2149.
[57] R. Wysokiński, D. Michalska, J. Comput. Chem. 22 (9) (2001) 901–912.
[58] R.W. Hay, T. Clifford, P. Lightfoot, Polyhedron 17 (20) (1998) 3575–3581.
[59] X. Jing-Yuan, G. Wen, L. Ling, Y. Shi-Ping, C. Peng, L. Dai-Zheng, J. Zong-Hui, J. Mol. Struct. 644 (2003) 23–27.
[60] A.E. Reed, L.A. Curtiuss, F. Weinhold, Chem. Rev. 88 (1988) 899.
[61] I. Fleming, Frontier Orbitals and Organic Chemical Reactions, Wiley, London, 1976.
[62] (a) Z.H. Abd El-Wahab, M.M. Mashaly, A.A. Salman, B.A. El-Shetary, A.A. Faheim, Spectrochim. Acta A 60 (2004) 2861–2873;
(b) N. Dharmaraj, P. Viswanathamurthi, K. Natarajan, Trans. Met. Chem. 26 (2001) 105–109.
[63] B. Tweedy, Phytopathalogy 55 (1964) 910.
[64] (a) K.N. Thimmaiah, G.T. Chandrappa, Rangaswamy, Jayarama, Polyhedron 3 (1984) 1237–1239;
(b) R.B. Johari, R.C. Sharma, J. Indian Chem. Soc. 65 (1988) 793–794.
[65] M. Pérez-Cabré, G. Cervantes, V. Moreno, M.J. Prieto, J.M. Pérez, M. Font-Bardia, X. Solans, J. Inorg. Biochem. 98 (2004) 510–521.